# Attosecond X-ray absorption fine-structure spectroscopy in condensed matter

by

**Bárbara Buades**

Thesis Advisor:
Prof. Dr. Jens Biegert

*A thesis submitted in fulfillment of the requirements*
*for the degree of Doctor of Philosophy*
*in the*

Attoscience and Ultrafast Optics



ICFO – Institut de Ciències Fotòniques
UPC – Universitat Politècnica de Catalunya

---

Barcelona, June 2018

# 4 Attosecond transient X-ray absorption fine-structure spectroscopy

*This chapter presents the first demonstration of attosecond-time-resolved electron dynamics involved during X-ray absorption fine structure spectroscopy (atto-tr-XAFS) under the influence of an IR laser pulse on a composed semimetal with proving an absorption edge in the SXR regime in the water window well above the carbon K-edge.*

*Firstly in Sec. 4.1 an introduction on how attosecond SXR pulses can be used to investigate ultrafast electron dynamics in composite materials through XAFS spectroscopy technique is presented. This time-resolved spectroscopic technique is applied to $TiS_2$ whose electronic properties are shown in Sec. 4.2. Afterwards the experimental configuration is detailed in Sec. 4.3 where electronic dynamics are pumped or trigged by a sub-2-cycle CEP-stable 1.85 $\mu$m pulse and probed or interrogated by the previously described generated attosecond pulse in the SXR regime in the water window. This is followed by Sec. 4.4 that presents a theoretical approach used to explain the electronic dynamics involved in the atto-tr-XAFS experiment. To extract more information about the electron dynamics in the femtosecond regime and optical properties of $TiS_2$, an optical pump/probe experiment is supplementary added in Sec. 4.5. This optical pump/probe experiment uses similar pumping wavelengths than the ones used in atto-tr-XAFS measurements but the probe pulse is now a 800 nm pulse with a pulse duration of a few tens of femtoseconds. Finally, the chapter ends with disclosing the conclusions from the experiments in Sec. 4.6.*

## 4.1 Introduction to attosecond transient XAFS in condensed matter

Microscopic insight into the position and the real-time motion of charge carriers close to the Fermi level in condensed phase is of fundamental importance for basic science as well as for the development of devices. These carriers most strongly interact with their environment and thus largely determine materials' optical and electronic properties and the functionality of devices made of these materials. Hence, access to the dynamics of these carriers is a long-standing goal of condensed matter physics to advance, for instance, computer processors whose speed and miniaturization has reached limits where further improvements are stymied without a comprehensive understanding of the dynamic many-body interactions of carriers[145,146]. Thus, knowledge about the space-time motion of carriers within a solid's band structure is essential to develop advanced materials for ultrafast electronics, batteries and energy converters, light harvesting compounds and information processing[147].

Earlier studies have applied time-resolved XAFS at SXR photon energies, but were limited to tens of femtosecond temporal resolution[148] incapable of grasping the sub-cycle electron dynamics. Attosecond transient XAFS (atto-tr-XAFS) was so far restricted to extreme ultraviolet (XUV) photon energies thereby limiting the applicability of the method to the study of only a few elements with suitable transitions energies[16,18,21,149–152], or to core-level dynamics[1,20]. Transferring the concept of atto-tr-XAFS to SXR photon energies in the water window covering the K-, L- and M-edge transition energies of more than 50 elements renders the method a powerful tool for the sub-optical cycle time-resolved study of charge dynamics in many more physical systems. In particular, the developments presented in our study turn light-field driven charge dynamics into an experimental observable by covering the relevant SXR transition energies at the $L_{2,3}$-edges of Titanium (460 eV) and Sulfides (160 eV), the $M_1$ and $M_{1,2,3}$-edges of the Selenides (230 and 166 eV, respectively), $N_1$-edge of the Tellurides (170 eV), and most importantly the strong K-edge of Carbon/Graphene (284 eV) and the Nitrides (409 eV).

Applying XAFS in crystalline matter, unlike atoms and molecules, have a continuum of energy states around the Fermi energy level due to the crystal periodicity[153]. Laser pulses with visible or infrared wavelengths, used as pump pulses, excite or initiate electron dynamics from states close to the Fermi level due to the low photon energy. In the simple picture of single photon absorption, the pump pulse leads to an electron transition from the valence band to the conduction band yielding to a new unoccupied DOS in the valence band and a new occupied DOS in the conduction band. XAFS, due to its element-specific and dipole transition character can only probe transitions within the same element and follow the se-

lection rules $\Delta l = \pm 1$. The first sample's requirement is that the transitions introduced by the pump pulse (in other words, the new unoccupied or occupied electronic DOS) can be access or probed by the attosecond SXR pulses.

As discussed in Chap. 3, the thickness of the sample must be such that the absorption edge jump under study is maximized. This typically implies a thicknesses below 200 nm which puts constrains on the availability of the samples since they must be manufacturable. However, thin samples have the advantage that the temporal smearing between the pump and probe pulses introduced by the group velocity dispersion difference is minimised. The approach here is to choose materials that are stable in a two dimensional configuration [154–157]. Although we require a desired thickness within a few tens of nanometers to less than 100 nm, this thickness is achieved by either exfoliation of the thick bulk crystal or slicing it using an ultra-microtome with a diamond blade. Table 4.1 shows the available layered materials with absorption edges at the water window that are sorted by the most prominent dynamics that can be probed by the attosecond SXR radiation source.

| **Layered material** | **Absorption edges energy (eV)** | **Direct bandgap** VB → CB | **Allowed transitions** $\Delta l = \pm 1$ |
|---|---|---|---|
| **Graphite** [119] | C K(284.2 eV) | Zero band gap | C 1s → VB&CB p-like |
| 100 nm | | C p-like → C p-like | |
| **BN** [158,159] | N K(410 eV) | 5.9 eV | N 1s → VB&CB p-like |
| 120 nm | | N+B p-like → N+B p-like | |
| **BCN** [160] | C K(284.2 eV) | 3 eV | C 1s → VB&CB p-like |
| 120 nm | N K(410 eV) | C p-like → C+N+B p-like | N 1s → CB p-like |
| **$TiS_2$** [143,161] | Ti $L_{2,3}$(460&454 eV) | 0.23 eV | Ti 2p → CB 3d-like |
| 70 nm | S $L_1$(231 eV) | S 3p-like → Ti 3d-like | S 2s → VB 3p-like |
| **$TiSe_2$** [161–163] | Ti $L_{2,3}$(460&454 eV) | 0.06 eV | Ti 2p → CB 3d-like |
| 70 nm | Se $M_1$(230 eV) | Se 4p-like → Ti 3d-like | Se 3s → VB 4p-like |

**Table 4.1: Sorted layered samples suitable for time-resolved XAFS in the water window**. The materials are sorted by the strongest absorption edge jump on the material to the weakest. The direct bandgap indicates the minimum photon energy the pump beam must contain to perform a direct single photon absorption from the valence band (VB) to the conduction band (CB). The SXR allowed transitions show the capability of detecting the induced electronic transitions around the Fermi level by the pump pulse within the same species of element. Strongest absorption edge jumps come from K, $L_{2,3}$, $M_{4,5}$ shells progressively in the atomic case, but here their absorption depends on the compound and the available states in the conduction band. Also the capability of measuring the absorption edge depends on the number of photons at the corresponding energy edge.

| Layered material | Absorption edges energy (eV) | Direct bandgap VB → CB | Allowed transitions $\Delta l = \pm 1$ |
|---|---|---|---|
| $TiO_2$ [164] 150 nm | Ti $L_{2,3}$(460&454 eV) | 3.02 eV O 2p-like → Ti 3d-like | Ti 2p → CB 3d-like |
| $VO_2$ [165] ($V_2O_5$) [166] 100 nm | V $L_{2,3}$(520&512 eV) | 0.67 eV (or 1.9 eV) O 2p-like → V 3d-like | V 2p → CB 3d-like |
| $VSe_2$ [167] 100 nm | V $L_{2,3}$(520&512 eV) Se $M_1$(231 eV) | 1.4 eV Se 4p-like → V 3d-like | V 2p → CB 3d-like Se, 3s → VB 4p-like |
| InSe [168] ($In_2Se_3$) [169] 70 nm | In $M_{4,5}$(464&456 eV) Se $M_1$(230 eV) | > 1.65 eV (or from 1.3 eV to 1.8 eV) Se 4p-like + In 5p-like→ Se 4s-like + In 5s-like | In 3d → VB 5p-like Se 3s → VB 4p-like No transition to CB |
| SnS [170] 50 nm | Sn $M_{4,5}$(493&484 eV) S $L_1$(231 eV) | > 1.65 eV S 3p-like → Sn 5s-like + S 3p-like | S 2s → VB&CB 3p-like |
| $MoTe_2$ [171] 70 nm | Mo, $M_{2,3}$(412&394 eV) Mo $M_{4,5}$(231&227 eV) | 1.23 eV Mo 4d-like + Te 5p-like → 0.75(Mo 4d-like)+0.25(S 3p-like) | Mo 3p → VB&CB 4d-like |
| $MoO_3$ [172] 70 nm | Mo $M_{2,3}$(412&394 eV) Mo $M_{4,5}$(231&227 eV) | 2.98 eV O 2p-like → Mo 4p-like | Mo 3p → VB&CB 4d-like |
| $MoS_2$ [173] 40 nm | Mo $M_{2,3}$(412&394 eV) Mo $M_{4,5}$(231&227 eV) S $L_1$(231 eV) | 1.74 eV 0.75(Mo 4d-like)+0.25(S 3p-like) → 0.9(Mo 4d-like)+0.1(S 3p-like) | Mo 3p → VB&CB 4d-like 2s → VB&CB 3p-like |
| $RuO_2$ [174] 40 nm | Ru $M_{2,3}$(484&461 eV) Ru $M_{4,5}$(284&280 eV) | Metallic 0.9(Ru 3p-like)+0.1(O 2p-like)→ 0.3(Ru 4d-like)+0.7(O 2p-like) | Ru 3p → VB&CB 4d-like |

**Table 4.1: Sorted layered samples suitable for time-resolved XAFS in the water window**. The materials are sorted by the strongest absorption edge jump on the material to the weakest. The direct bandgap indicates the minimum photon energy the pump beam must contain to perform a direct single photon absorption from the valence band (VB) to the conduction band (CB). The SXR allowed transitions show the capability of detecting the induced electronic transitions around the Fermi level by the pump pulse within the same species of element. Strongest absorption edge jumps come from K, $L_{2,3}$, $M_{4,5}$ shells progressively in the atomic case, but here their absorption depends on the compound and the available states in the conduction band. Also the capability of measuring the absorption edge depends on the number of photons at the corresponding energy edge.

| Layered material | Absorption edges energy (eV) | Direct bandgap VB → CB | Allowed transitions $\Delta l = \pm 1$ |
|---|---|---|---|
| $ZrS_2$ [175] 40 nm | Zr $M_1$(430 eV) Zr $M_{2,3}$(344&330 eV) S $L_1$(231 eV) | 1.7 eV S 3p-like → Zr 4d-like | Zr 3p → CB 4d-like S 2s → VB 3p-like |
| $NbS_2$ [176] 50 nm | Nb $M_1$(466eV) Nb $M_{2,3}$(376&361 eV) S $L_1$(231 eV) | Metallic 0.25(S 2p-like)+0.74(Nb 4d-like) → S 2p-like + Nb 4d-like | Nb 3p → CB 4d-like S 2s → VB 3p-like |
| $NbSe_2$ [177] 50 nm | Nb $M_1$(466eV) Nb $M_{2,3}$(376&361 eV) Se $M1_1$(230 eV) | Metallic 0.2(Se 3p-like)+0.8(Nb 4d-like) → Nb 4d-like | Nb 3p → CB 4d-like Se 3s → VB 4p-like |
| $HfS_2$ [178] 30 nm | Hf $N_{2,3}$(438&381eV) S $L_1$(231 eV) | 3.6 eV S 3p-like + Hf 5d-like → Hf 5d-like | Hf 4p → VB 5d-like S 2s → VB&CB 3p-like |
| $WS_2$ [171] 20 nm | W $N_{2,3}$(490&423eV) S $L_1$(231 eV) | 2 eV S 3p-like + W 5d-like → 0.25(S 3p-like)+0.75(W 5d-like) | W 4p → VB&CB 5d-like S 2s → VB&CB 3p-like |

**Table 4.1: Sorted layered samples suitable for time-resolved XAFS in the water window**. The materials are sorted by the strongest absorption edge jump on the material to the weakest. The direct bandgap indicates the minimum photon energy the pump beam must contain to perform a direct single photon absorption from the valence band (VB) to the conduction band (CB). The SXR allowed transitions show the capability of detecting the induced electronic transitions around the Fermi level by the pump pulse within the same species of element. Strongest absorption edge jumps come from K, $L_{2,3}$, $M_{4,5}$ shells progressively in the atomic case, but here their absorption depends on the compound and the available states in the conduction band. Also the capability of measuring the absorption edge depends on the number of photons at the corresponding energy edge.

The more compounds a material has, the weaker the absorption jump at the edge is and more challenging the XAFS measurement becomes. For example, perovskite-type materials such us $Ca_2Ta_2TiO_{10}$, $Bi_4Ti_3O_{12}$, $Sr_2Nb_3O_{10}$ and $LaNb_2O_7$ with thicknesses of 400 nm, 70 nm, 200 nm and 100 nm, respectively, lead to a jump of around 10% at the titanium $L_{2,3}$ and at the niobium $M_{2,3}$ edges with a total transmission of only 50%. It is worth mentioning that although those materials might contain strong absorption edges ($L_{2,3}$) due to the weak contribution of those elements in the material the absorption edge jump becomes weaker.

Other crystal materials such as SiC, $Si_3N_4$, InN, GaN, InGaN and InAs can

be obtained either by vapour depositing them on a thin substrate or by reducing their thickness using an ion beam. The issue of vapour deposition is that it needs a substrate with a flat absorption across the water window spectral region such as Si, $SiO_2$, $Al_2O_3$ GaAs, Cr or Al. This substrate must be thin and checked to ensure that it does not change the electrical properties of the sample under study. Another drawback of vapour deposition is that it typically leads to samples with nano-crystalline domains that are oriented randomly across the probed sample area, losing the possibility of orbital probing by changing the linear polarised electric field projection onto the orbital. On the contrary, using an ion beam to reduce the thickness of the bulk material can be time consuming since the reduction can happen from a few micron to tens of nanometres across a the entire probed sample which is desired to have a diameter of a hundred microns. In addition, this sputtering technique is not suitable for composite materials since this process might change the local composition of the sample.

Another feature to consider when choosing the sample under study is the capability of inducing an efficient electron dynamic without requiring a strong pump fluence. In semiconductors, this comes down to inducing single photon absorption with photon energies slightly higher than the band gap energy. In metals other electron dynamics such as intra-band electron density re-distribution are induced which put no strict requirement on the pump photon energies. Moreover, the sample must be stable, in other words, the sample properties must recover after being pumped before the next pump pulse comes. At 1 kHz repetition rate of the pump and probe pulses, the recovery must happen within 1 ms.

## 4.2 $TiS_2$

Especially relevant in this context of layered materials for which titanium disulfide ($TiS_2$) is an example being a semi-metallic transition-metal dichalcogenide compound, which exhibits high carrier mobility and energy storage capability[108,179,180]. $TiS_2$ is of interest for solid batteries[181–183] and it is discussed as a platform for ultrafast optoelectronic devices and field-effect transistors[184,185]. Intercalation can tailor the material's conductivity[186], and compressive strain can mediate a transition from metallic to an excitonic insulator phase[187]. To date, this array of possibly trendsetting properties is widely explored despite the difficulties to gain insight into the materials real-time and space electron dynamics.

Figure 4.1 shows the tri-layered structure of 1T-$TiS_2$ consisting of hexagonal sheets of cationic $Ti^{4+}$ atoms sandwiched between sheets of S atoms. The atoms within the tri-layers (S-Ti-S) are covalently bonded while the tri-layers are coupled

between each other by weak Van der Waals forces[179].

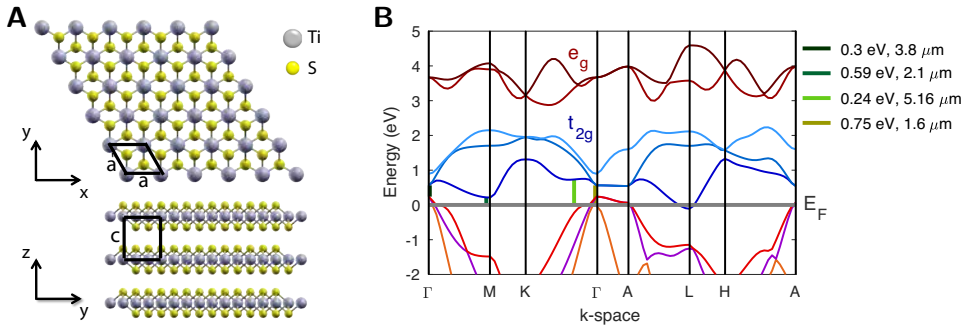


**Fig. 4.1: $TiS_2$ structure.** (**A**) Titanium atoms are sandwiched by sulfur atoms to form $TiS_2$ layers with hexagonal symmetry. Each layer is coupled to each other by Van der Waals forces. a = 3.36 Å and c = 5.70 Å. (**B**) $TiS_2$'s band structure around the Fermi energy level ($E_F$) showing the $t_{2g}$ and $e_g$ band manifolds. Also shown are the direct transitions from the maximum of the valence band to a flat region of the conduction band.

Investigations of the material's properties triggered long-lasting controversies from the 60's to the 80's of whether the material is semimetallic or semiconductor[161,188,189]. This discrepancies came mainly due to impurities on the material that could shift the Fermi level up or down. Nowadays it is possible to obtain $TiS_2$ much more purified leading of no such controversies. Recent theoretical and experimental studies converge on the semimetallic behaviour with high anisotropic properties of $TiS_2$ and its transition to semiconductor with the presence of applied pressure or strain[179,180,185,187,190,191]. Consistent with these previous works, Fig. 4.1 also shows the semi-metallic band structure of bulk 1T-$TiS_2$ calculated from first principles in the framework of density-functional theory[192,193], as implemented in the all-electron full-potential code exciting[194] (see Sect. 4.4). The hexagonal non primitive unit cell has the same reciprocal directions as the graphite, shown in Fig. 3.2.

### 4.2.1 Sample growth

Single crystals of $TiS_2$ with low impurity concentration are grown by Chemical Vapor Transport (CVT) of the prereacted stoichiometric material using iodine as a transport agent. First of all, the polycrystalline material is synthesized by mixing in a stoichiometric ratio powders of Ti (99.98% from Sigma-Aldrich) and S (99.98% from Alfa-Aesar). The mixture is sealed in an evacuated quartz ampoule ($P \approx 5{\cdot}10^{-5}$ mbar, length = 25 cm, internal diameter = 1.5 cm) and heated from room temperature to 910°C at 5°C/min. Then, the temperature is kept constant for 9 days and cooled down naturally. Secondly, 4 mmol of the previous material is

mixed with iodine as a transport agent ($[I_2] \approx 5$ mg/cm$^3$) in an evacuated quartz ampoule (P $\approx 7{\cdot}10^{-6}$ mbar, length = 50 cm, internal diameter = 1.5 cm). The ampoule is placed inside a three-zone furnace with the material in one side. The other two zones are heated up from room temperature to 700°C at 4°C/min and kept at this temperature for two days. After this, the zone with the material is heated up to 750°C in 3 hours and it is established with gradient of 50°C between the hot and cold zones. Then, the temperature is kept constant for 15 days and cooled down naturally.

The obtained crystals are analysed by Inductively Coupled Plasma mass spectrometry (ICP), elemental analysis and X-ray powder diffraction (XRPD). The percentage proportions of elements obtained is Ti: (43 ± 2)% and S: (58 ± 1)%, in good agreement with the expected ones (Ti: 42.7%, S: 57.3%). The refinement of the X-ray pattern (Fig. 4.2) revealed a trigonal crystal system with a P-3m1 space group and a unit cell determined by $\alpha = \beta = 90$ deg. and $\gamma = 120$ deg. and a = b = 3.4078(4) Å and c = 5.6999(8) Å, in good accordance with the values reported in the literature[195].

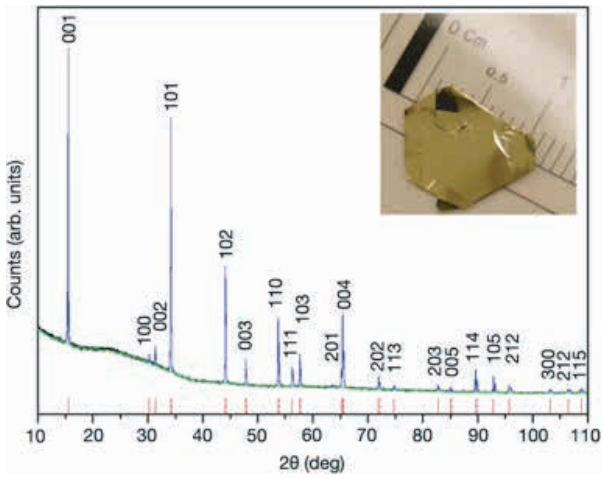


**Fig. 4.2: $TiS_2$ crystalline structure analysis.** XRPD experimental pattern (black) and corresponding fit (peaks in blue and background in green) for a $TiS_2$ crystal. For simplicity, the peaks position have been marked with red lines. The fit gives as a result: a = b = 3.4078(4) Å and c = 5.6999(8) Å, $\alpha = \beta = 90$ deg. and $\gamma = 120$ deg., trigonal crystal system with P-3m1 space group, $\chi^2 = 1.9{\cdot}10^{-6}$ and a Snyder's figure of merit of 39.72[196]. Inset: Photograph of a $TiS_2$ crystal.

### 4.2.2 Sample preparation

Since the grown single crystal is too thick for an X-ray absorption measurement an ultra-microtome with a diamond blade is used to cut 150 nm thin sheets of the

crystal with a surface area of several-hundred-micron diameter. These thin sheets are mounted on a 3 mm-diameter 20 $\mu$m-thick TEM grid made of copper with a square mesh whose pitch is 125 $\mu$m with bars 35 $\mu$m wide. Thus, clear areas of 90 $\mu$m x 90 $\mu$m are accessible for measurements with a freestanding sample. Figure 4.3(A) shows a microscope image of the TEM grid with a $TiS_2$ sheet.

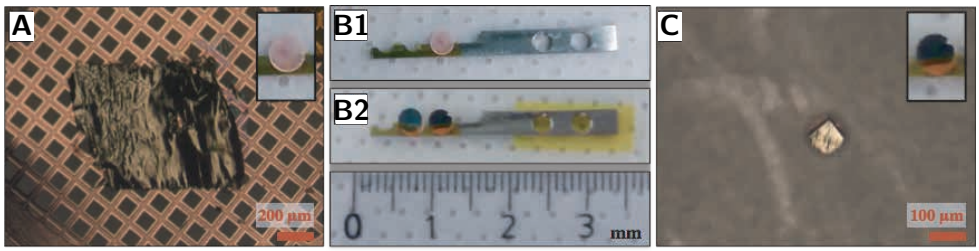


**Fig. 4.3: Assembly of the $TiS_2$ samples.** (**A**) shows the TEM grid with a 150 nm thin $TiS_2$ sheet mounted on top. (**B1**) shows the $TiS_2$ target on top of the TEM grid mounted on the sample holder. (**B2**) shows the final assembly of two targets with 100 $\mu$m ID disc mounted on top. (**C**) shows a view through the nickel disc with the $TiS_2$ sample sandwiched between TEM grid and disc.

The TEM grid with the $TiS_2$ sample is then transferred to the sample holder (Fig. 4.3(B1)) and a nickel disc with ID of 100 $\mu$m is placed on top over an area of the $TiS_2$ sample which is homogeneous, flat and provided maximum clearance between the TEM grid's bars - see Fig. 4.3(B2). The disc also insures the maximum spatial overlap between both pump and probe beams. The zoomed-in image in Fig. 4.3(C) shows a view through the hole of the disc. Visible is the $TiS_2$ sample and part of the TEM grid. The outer diameter of the disc is much larger than any of the beams which ensures that only the 100 $\mu$m hole transmits the pump and probe through the sample. The disc has a thickness of $\approx$ 20 $\mu$m which is sufficiently large to block any transmission of the SXR radiation. Furthermore, since the sample is placed at the entrance-slit plane of the flat field spectrograph, the disc hole defines the entrance slit of the spectrograph.

## 4.3 Attosecond transient XAFS in $TiS_2$

Here, broadband soft X-ray attosecond-duration light pulses[39,40] provide unique insight into the instantaneous response of the material to the external stimulus by an electric field, and the subsequent charge carrier dynamics set in motion by the light-field.

AttoXAFS is used to interrogate the DOS in the complex material of $TiS_2$ close to the Fermi level through X-ray-induced dipole transitions from localized

Ti-2p core states ($L_{2,3}$ edge at $\approx$ 460 eV) to non-fully-occupied bound states[197] positioned in the energy band structure in the proximity of the Fermi level and to the continuum. This attoXAFS is ideally suited for time-resolved measurements as the method takes full advantage of the tremendous spectral bandwidth[95] of attosecond pulses in single-shot detection[55]. Another important aspect in disentangling the contributions of the various constituents of composite materials is achieving element selectivity[198,199], which is realized with soft to hard X-ray photons driving transitions between well-localized core electronic ground states and states in the conduction band manifold of a solid.

In this first implementation of sub-optical cycle time-resolved XAFS spectroscopy at SXR photon energies the potential of the methodology is demonstrated by resolving the motion of charge carriers in real-time inside the complex semi-metallic bandstructure of the binary transition-metal dichalcogenide material $TiS_2$.

Figure 4.4 illustrates the concept underlying the experiments. The angular momentum character of the valence bands are a mix of sulfur p and s states, while the conduction bands are predominantly titanium d states. The material's semi-metallic character originates from the DOS at the Fermi energy consisting predominantly of overlapping sulfur p states (valence) and titanium d states (conduction) at the L point. The attosecond SXR pulse's spectrum comprised photon energies ranging from 200 to 550 eV, which permits accessing the 2p core states in Ti with a binding energy of 458.4 eV ($2p_{3/2}$) and 465.5 eV ($2p_{1/2}$) and hence a direct interrogation of the dipole-allowed core-level transition into conduction band states of predominantly Ti-3d character.

In the experiment, linearly-polarized, isolated sub-300-as-duration SXR pulses[39,40], their duration corresponding to $\approx 1/20$th of the optical cycle of the IR pump field, are used at 30 deg. incidence with respect to the basal plane normal of a 150 nm-thin, free-standing, mono-crystalline 1T-$TiS_2$ membrane to sample the entire k-space. The transmitted spectrum is acquired at once using a dispersive X-ray spectrograph, (see Sec. 1.2 for more details on the SXR detection).

For the time-resolved experiment, charge carrier dynamics are stimulated by irradiating the material with a CEP-stable sub-2-cycle-duration (12 fs at FWHM) laser pulse at a centre wavelength of 1.85 $\mu$m (0.6 eV). The pump pulse is a low-energy replica of the CEP-stable high-energy pulse that produces the isolated attosecond SXR pulse through high harmonic generation. The pump pulses are synchronised with the attosecond SXR pulses using a linear stage with sub-nm resolution[39,40,74]. More details of the setup are described in Chap. 1, Sec. 1.3 where the sample is tilted 30 deg. from the basal plane respect to the SXR beam.

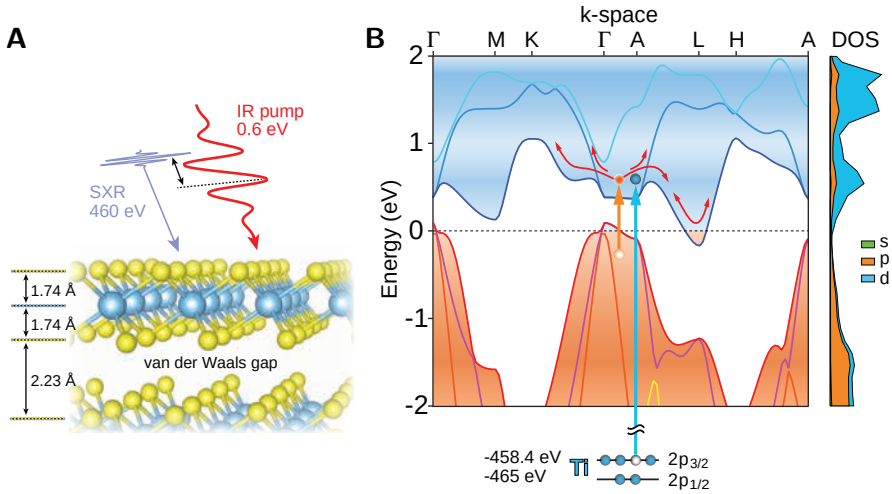


**Fig. 4.4: Attosecond transient X-ray absorption spectroscopy on $TiS_2$.** (**A**) A sub-2-cycle 1.85 $\mu$m pump pulse stimulates carrier dynamics inside a 150 nm-thin $TiS_2$ crystal (sketched are two layers), which is probed by a sub-300-as-duration SXR pulse in small-angle non-collinear geometry. (**B**) shows the relevant band structure of the $TiS_2$ semimetal together with IR induced excitation pathways and the accessible core transitions. The attosecond SXR pulse invokes $L_{2,3}$ transitions from titanium 2p core orbitals into conduction band states which are predominately of Ti-3d character.

The pump beam is incident with a slightly non collinear angle with the SXR beam onto the sample at 26.3 deg. with respect to the basal plane normal. The refractive index of $TiS_2$ is highly anisotropic for fields along the x and z axes which are the axes along and perpendicular to the sample plane, respectively. Three different literature values are taken [180,200,201] for the different refractive indexes to calculate the resulting refractive index along the relevant propagation direction inside the material. Since the computed values range between 4.97 to 5.01 and 5.70, a mean value of $5.2 \pm 0.3$ is considered. Using this value for propagation at 1.85 $\mu$m and $n = 1$ at 460 eV, the 1.85 $\mu$m pump beam is calculated to propagate at 5.5 degree off the surface normal inside the material while the SXR beam does not undergo any significant refraction.

The spectrum of the sub-2-cycle pump pulse spans photon energies ranging from 0.5 to 1 eV capable of driving single photon transitions between valence and conduction band states separated at the $\Gamma$ point by 0.23 eV. To determine the excitation field strength, we measure the energy of the pump at the target location. Due to several reflections on silver-coated mirrors the energy is reduced to $(4.8 \pm 0.5)$ $\mu$J. Since propagation occurred entirely under vacuum, we assume the measured pulse duration of 12 fs at FWHM which, together with the measured

beam profile, yields an estimated vacuum peak intensity at the target of (8.4 ± 1.7)·$10^{11}$ W/$cm^2$. Based on the refractive index values, the Fresnel losses at the interface of (51 ± 2)% reduces the peak intensity to (4.1 ± 0.8)·$10^{11}$ W/$cm^2$ or an excitation field strength of (0.077 ± 0.008) V/Å inside the material. This field strength inside the material corresponds to an excitation of approximately 0.03 electrons per unit cell[1].

### 4.3.1 Static attoXAFS at the Ti $L_{2,3}$ edges

First of all, a static attoXAFS measurement at the Ti $L_{2,3}$ edges, i.e. unpumped and non-time-resolved, is carried out to compare it with theory as well as with measurements performed using synchrotron radiation in the BL29 BOREAS beamline at the ALBA synchrotron in Barcelona, Spain. Although a more accurate comparison between attoXAFS and XAFS using synchrotron radiation is shown in the previous section 3.3.2, here the acquisition of the attoXAFS data is presented. The capability of resolving $L_2$ and $L_3$ edges of titanium in the $TiS_2$ material is also demonstrated. Figure 4.5 shows the raw spectrograph image of the SXR radiation through the sample with a 150 nm thick $TiS_2$ which can be compared with the signal acquired in the spectrograph without a sample shown in Fig. 1.5, Chap. 1.

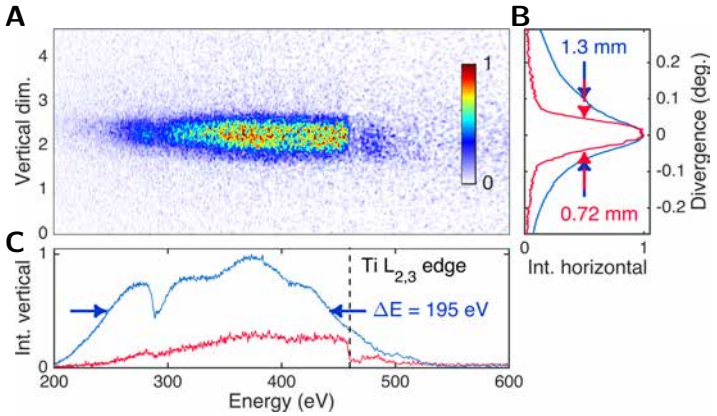


**Fig. 4.5: Dispersive attoXAFS measurements with the spectrograph on $TiS_2$.** (**A**) shows the vertical extent of the SXR beam on the spectrograph camera after being transmitted through the $TiS_2$ sample. (**B**) and (**C**) compare the beam divergence and beam spectrum, respectively, of the SXR beam with (red) and without (blue) being transmitted through the sample. Immediately visible is a reduction in the overall SXR counts and also a sharp drop of the SXR counts above the Ti L edges. Clearly visible is residual carbon absorption at the k-shell edge at 284 eV.

[1] Absorption coefficient used for the calculations is taken from Ref. Feldkamp et al., 1979 [202].

The vertical spatial extent of the beam through the sample is reduced by the 100 $\mu$m pinhole from 1.3 mm to 0.72 mm. The attosecond SXR spectrum with a width of 195 eV is affected by the absorption response of the $TiS_2$ compound. Still visible is the ubiquitous absorption at the carbon K-shell edge at 284 eV originating from small hydrocarbon contamination of the beamline due to the usage of turbo pumps. Upon inserting the sample, the spectral transmission decreased and the Ti edge became clearly visible. The spectrum is obtained by vertically integrating the signal on the CCD camera chip. From both spectra (with and without the sample) taking the ratio and logarithm, the optical density is extracted.

Figure 4.6 shows the XANES or NEXAFS at the Ti $L_2$ and $L_3$ absorption edges (corresponding to Ti $2p_{1/2}$ and $2p_{3/2}$ to 3d states transitions, respectively) obtained from the attoXAFS measurement in addition to a measurement of the TEY signal recorded at the ALBA synchrotron. The synchrotron measurement has a much higher resolving power (>10000) and is based on a monochromatized SXR beam of tunable energy which is scanned from 450 to 490 eV. Overlaid are calculations using Bethe-Salpeter equation (BSE) with excitonic effects included[203]. The $Ti^{4+}$ $d^0$ ground state makes it a particular case among transition elements: its X-ray absorption spectrum across the $L_{2,3}$ edges becomes proportional to the conduction band-DOS thus easing spectral interpretation. The attoXAFS spectra is recorded in 8 min acquisition time. Both the TEY and calculated spectra are shifted towards higher energies to match with the attoXAFS spectrum.

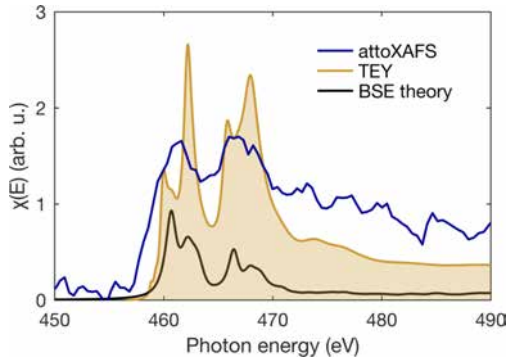


**Fig. 4.6: Comparison between attoXAFS, TEY and theory.** It shows the attoXAFS signal of $TiS_2$ at the titanium $L_{2,3}$ absorption edges measured simultaneously with the SXR attosecond pulses at normal incidence (blue). Overlaid are the TEY (orange) measured at the synchrotron beamline and also the result from a calculation (black) based on DFT[192,193] using the Bethe-Salpeter equation (BSE) with excitonic effects included[203]. The high resolution of the spectrograph allows the $L_2$ and $L_3$ edges to be distinguished clearly. The synchrotron spectrum is shifted by 5 eV towards higher energies to match the attoXAFS spectrum.

### 4.3.2 Data acquisition of attosecond transient XAFS

As previously shown, to attosecond time-resolve electron dynamics induced by the pump pulse, this pulse is synchronised with the sub-300-as-duration SXR probe pulse using a delay stage with sub-nanometre resolution and spatial overlap on a 100 $\mu$m diameter sample. The SXR radiation through the sample is spectrally resolved under the influence of the pump pulse.

The pump-probe delay is initially scanned in rough temporal steps of 1 to 3 fs to establish the exact temporal location of the absorption signal. In the following, a negative delay signifies that the attosecond SXR probe pulse arrives before the pump pulse. Consequentially, a positive delay means that the material is excited and the probe interrogates this excitation. We note that the zero-delay position is arbitrarily chosen at the temporal overlap with the maximum intensity of the pump pulse. The measurement proceeds by scanning over early delays in fine steps of 100 as (at the start of the pump pulse) with the intention to resolve the build-up of the material excitation. Later delays are scanned in steps of 200 as. The absorption signal is integrated on the CCD camera over 6 min for the earlier (100 as delay step) scan and 5 min for the later (200 as delay step) scans. At each time step, the spectrum of the atto-SXR pulse is recorded twice before incrementing the delay, first without the presence of the pump pulse and consecutively with the presence of the pump. Although the CEP of the driving laser of HHG is actively locked resulting in a constant spectral shape of the SXR spectra, recording the unpumped signal at each time delay confirms that viewed changes come from the pump influence and not from intrinsic spectral deviations on the source. Figure 4.7 shows pumped (A) and unpumped (B) transmission for the covered pump-probe delay; blanked out are areas for which data is not recorded. The spectrograph covered a photon energy range from 173 to 974 eV, and the relevant Ti L-edge XANES within a window of photon energies ranging from 420 to 490 eV are shown.

To highlight changes at or around the absorption edge, we apply a local regression using weighted linear least squares and a 2nd degree polynomial model that assigns lower weight to outliers in the regression and also eliminates outliers which deviate in value more than six times the mean value. Raw absorption spectra (blue) together with the filtered ones (red) are shown in figure 4.8 at different time delays.

It is worth noticing that in both the raw data and filtered data there is a clear drop in transmission at energies above the absorption edge. However, the distinguishability between the $L_2$ and $L_3$ edges of titanium is only present in the raw data. Filtering the spectra reduces the energy resolution to $\pm$ 2 eV at 460 eV, though highlighting the temporal changes. In addition, to compensate the lower

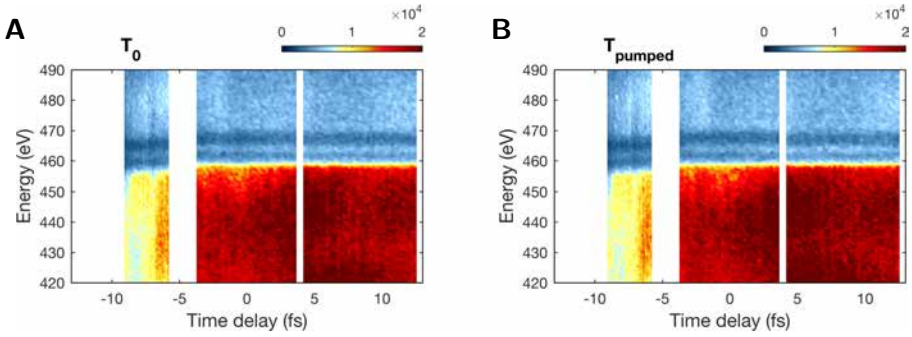


**Fig. 4.7: Measured transmission spectra for attosecond time resolved XAFS in $TiS_2$.** Detected counts of the transmitted attosecond soft X-ray through 150 nm $TiS_2$ as a function of the delay between pump and probe beam for 3 different scans along the pump pulse. Positive delays correspond to the pump pulse arriving before the SXR probe pulse. $T_0$ is the reference signal without the influence of the pump (**A**), and $T_{pumped}$ shows the pump influence on the sample (**B**). At each delay time the spectrum is integrated over 6 minutes with a delay step of 100 as for the range earlier than -5 fs, and integrated over 5 minutes with a delay step of 200 as at later delay times.

signal to noise ratio (SNR) in the scan at the start, the transmitted spectra is averaged over the previous and consecutive spectra as a function of the delay, yielding to an improvement in the SNR at the expense of temporal resolution. The resulting absorption spectra for the entire pump - probe delay scan are shown in Fig. 4.9.

Figure 4.10 shows differential transmission filtered spectra normalized to the static (unpumped) case, as a function of IR-pump attosecond-SXR-probe delay. Immediately noticeable are strong oscillations in the differential transmission and

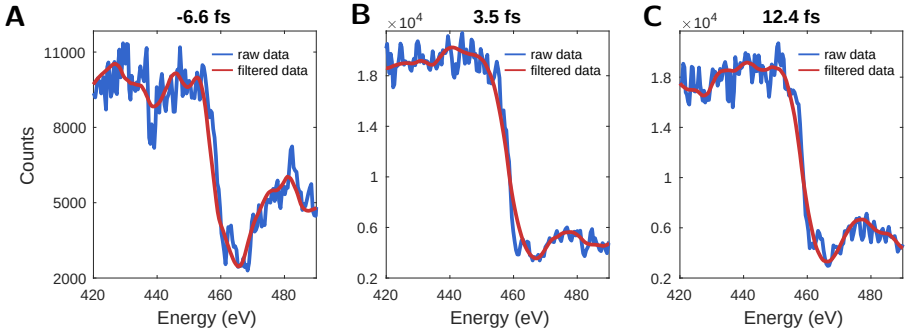


**Fig. 4.8: Spectral filtering of the raw data.** Shown is the effect of filtering (red) on the raw data (blue) for line-outs from the reference signal $T_0$ shown in Fig. 4.7 at time delays of -6.6 fs (**A**), 3.5 fs (**B**) and 12.4 fs (**C**).

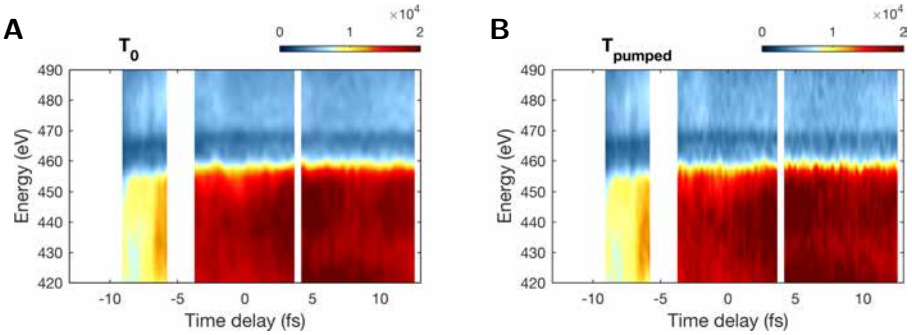


**Fig. 4.9: Filtered attosecond transient XAFS in $TiS_2$.** Shown are the unpumped (**A**) and pumped (**B**) transmitted spectra with the spectral filter function applied and temporal averaging from the raw data shown in Fig. 4.7.

values which turn positive (red) but also negative (blue) with twice the pump laser's periodicity, $2\omega_L$. Note that positive and negative values report an increase and a decrease in transmission due to the pump-laser-induced excitation of the material, respectively.

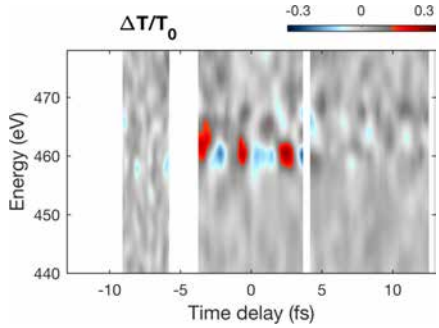


**Fig. 4.10: Attosecond transient soft X-ray absorption and carrier dynamics.** Shown are the differential SXR filtered spectra as a function of pump-probe delay. $\Delta T$ is normalized to the unpumped case $T_0$ for each time delay. Clearly visible are sub-cycle oscillations of negative and positive differentials.

The transmission of the attosecond SXR is chosen to be presented for the analysis and not the absorption as reflectivity is significant, (51 $\pm$ 0.02)%, thus the simple relation $A = 1 - T$ would not be justified; $A$ being the absorption. Considering dipole selection rules for the SXR core transitions from Ti-2p states, which exclusively interrogate conduction band states (Ti-3d character), an increase of electronic density (at a given k-point) would directly result in decreased absorption or increased transmission due to Pauli blocking[204]. Figure 4.11 shows the energy position of the strongest changes induced by the pump pulse found at the middle of the tr-XAFS scans. The $\Delta T/T_0$ changes are overlaid with the static XANES spectrum of the titanium $L_{2,3}$ absorption edges previously shown in Fig. 4.6.

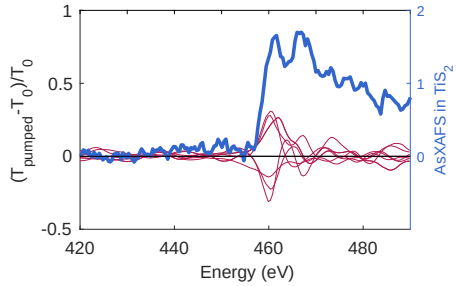


**Fig. 4.11: Energy decipher of induced temporal transmission changes.** Shown are the spectral position of the strongest induced changes of the pump pulse found in the middle of the tr-XAFS scan. The XANES spectrum is overlaid to identify the relative maxima or minima spectral changes which happen to be at the lower energy part of absorption edge of the Ti $L_{2,3}$.

The energy calibration of each measured section of the spectra has been carefully validated by comparing the derivative of the unpumped absorption signals. The position of the maximum of the derivative is related to the position of the absorption edge jump. This position does not change along the measurement for the unpumped signal. However, the applied filter is dependent on signal changes above and below the absorption edge, leading to a slightly change on the position of the maximum of the derivative signal as a function of time and depending on the scanned range. Figure 4.12 shows the spectral derivative at different time delays across the time-resolved scan for the raw data and the filtered data. To apply a spectral derivative to the raw data, the data is first corrected with a gentle smoothing over 10 energy pixels ($< 1$ eV) to avoid artefacts.

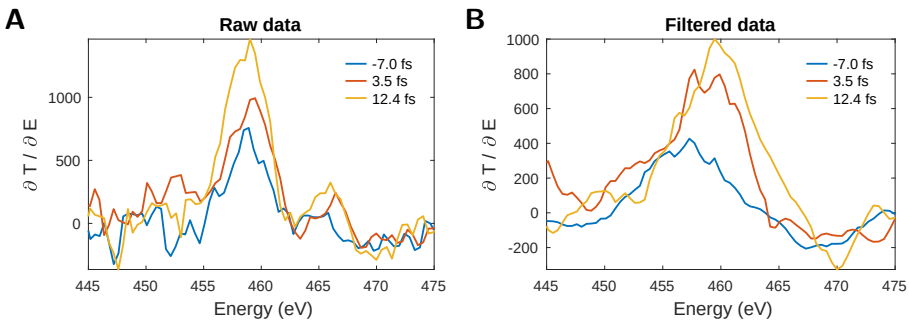


**Fig. 4.12: Spectral derivative of the transmitted signal.** Shown are the spectral derivatives for the raw data (**A**) and filtered data (**B**) (from Figs. 4.7 and 4.9, respectively) around the absorption edge for 3 temporal delays. The delays are taken at the start, middle and end parts of the atto-tr-XAFS scan.

Figure 4.13 shows the changes between the pumped and unpumped spectral derivatives of the measured transmission. The main changes can be identified around 456 eV, 462 eV and 467 eV. The changes at 456 eV are clearer in the

differentiated signal $((\partial T_{pumped}/\partial E)$ - $(\partial T_0/\partial E))$, more clearly visible at the middle part of the scan where the changes are maximum. The periodicity of the positive and negative changes is again around 3 fs which corresponds to a $2\omega_L$ component. The changes at 462 eV and 467 eV are more visible in the divided signal $((\partial T_{pumped}/\partial E)$ / $(\partial T_0/\partial E))$ where the oscillations are still visible but with a much worse signal to noise ratio. Dividing the pumped signal by the unpumped signal shows relative changes by highlighting changes where the absolute signal is smaller.

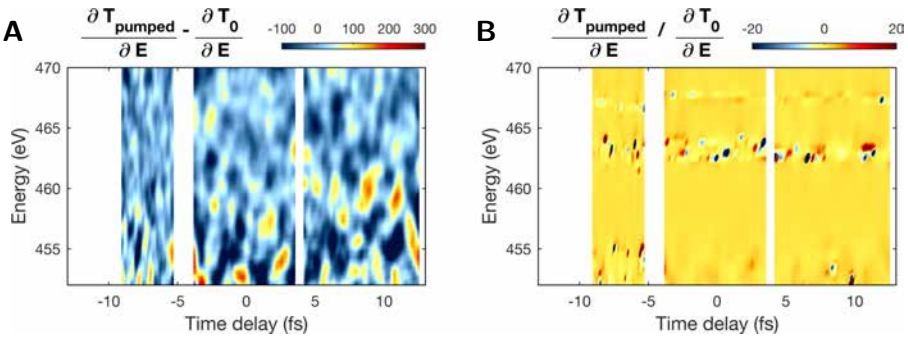


**Fig. 4.13: Temporal changes in the spectral derivative of the measured transmission.** (**A**) shows the differentiated derivatives, $((\partial T_{pumped}/\partial E)$ - $(\partial T_0/\partial E))$, and (**B**) shows the divided derivatives $((\partial T_{pumped}/\partial E)/(\partial T_0/\partial E))$. The derivative is applied to the corrected raw atto-tr-transmitted data shown in Fig. 4.7. The main oscillating changes at $2\omega_L$ appear around 456 eV (prominent in the scanned section at the middle part of the pump pulse), around 463 eV and 467 eV.

Thanks to the applied filter to the transmission, the spectral changes caused by the pump pulse can be identified in time. Adding the spectra corresponding to the time frames at the maximum change, minimum change and zero change, one can get back the spectral resolution and be able to spectrally resolve the changes. Figure 4.14 shows the average of these spectra and how a positive change appears at 456 eV at delays of -3.5 fs, -0.5 fs and 2.5 fs, it becomes negative at delays of -2.14 fs, 0.3 fs and 3.7 fs and disappears at delays of -1.3 fs, 0.2 fs and 3.2 fs.

Although the data has still a significant amount of noise, an overall signal can be distinguished. There is a dominant positive change induced by the pump spectrally averaging over the delays where the signal is expected to have a maximum change strength, seen in Fig. 4.14(A). The same happens with an expected negative change and no change shown in Figs. 4.14(B) and 4.14(C), respectively. This oscillating signal from positive to negative is found at the proximities of the titanium absorption edges $L_{2,3}$. Here, it is indicated that the predominant changes induced by the pump pulse are around 456 eV, 463 eV and 467 eV. This is in agreement with the changes found in the spectral derivative from Fig. 4.13.

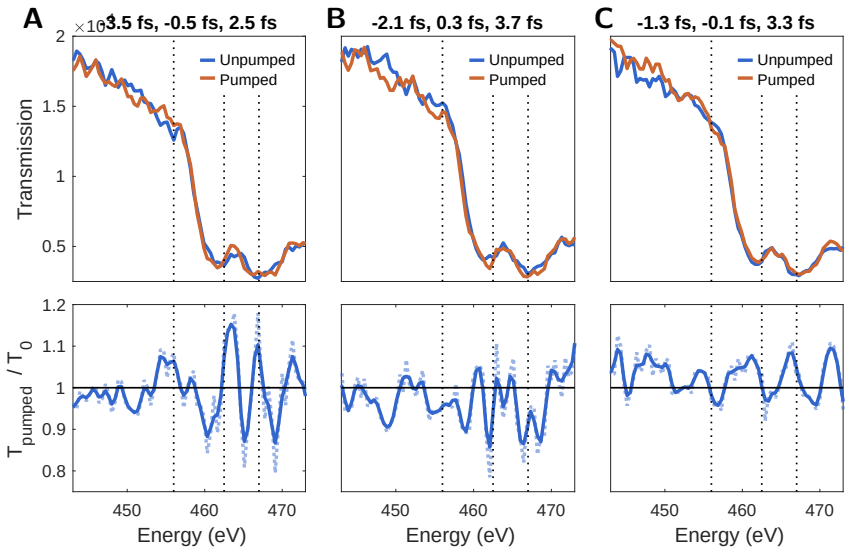


**Fig. 4.14: Transmission at delays with maximum induced changes.** Shown is the average over the raw data of the pumped and unpumped transmitted signal at the positions where induced changes are maximum (**A**) at delays of -3.5 fs, -0.5 fs and 2.5 fs, minimum (**B**) at delays of -2.14 fs, 0.3 fs and 3.7 fs, and zero (**C**) at delays of -1.3 fs, 0.2 fs and 3.2 fs. A dotted black line is used as a guide to indicate the spectral changes at 456 eV, 462.5 eV and 457 eV. Underneath the transmitted signal, the divided $T_{pumped}$ by $T_0$ signal is displayed to show the relative spectral changes.

Additionally, a more accurate frequency analysis of the filtered atto-tr-XAFS data presented in Fig. 4.10 is conducted which is shown in Fig. 4.15. A clear $2\omega_L$ component of the oscillating transient absorption changes is found together with a component oscillating at approximately three-times the pump laser frequency, $3\omega_L$. The $2\omega_L$ component is connected to changes proportional to the amplitude of the pump electric field whereas the $3\omega_L$ component is possibly connected to the onset of period breaking of the intra-band driven carrier motion ultimately leading to the emission of high-harmonic radiation [205].

The three atto-tr-XAFS scans that probe different parts of the pump electric field are put together under 2 considerations: 1) the changes must be present within 12 fs time delay and 2) the oscillations must be preserved with a $2\omega_L$ frequency component strongly shown in the middle part of the pump pulse where the electric field amplitude is maximum. The first consideration is based on a continuous scan performed across the entire pump probe temporal overlap. To find the region of pump probe temporal overlap, different scans with course step size between 1 and 3 fs are made. Figure 4.16 shows the spectral derivative of the transmitted transient changes of this rough scan evidencing the envelope of the

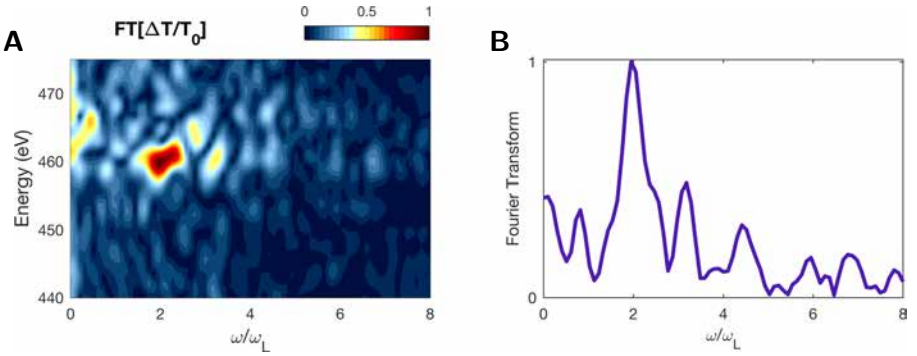


**Fig. 4.15: Spectral frequency analysis of the filtered atto-tr-XAFS in $TiS_2$.** (**A**) shows the normalized Fourier Transform (FT) of the time resolved transmission changes ($T_{pumped}$ - $T_0$)/$T_0$ (Fig. 4.10) which is spectrally decomposed. (**B**) shows the integration of the FT across the oscillating transient spectra from 456.9 eV to 461.6 eV. The main frequency components appear at $2\omega_L$, where $\omega_L = 1$ fs$^{-1}$ is the central frequency of the pump laser pulse which corresponds to 1.85 $\mu$m central wavelength. There is also a small $3\omega_L$ contribution.

changes introduced by the pump pulse on the $TiS_2$ sample with a FWHM = (12 $\pm$ 4) fs. The derivative analysis is performed after filtering due to the low signal to noise ratio of the rapid scan with coarse delay, but it allowed us to narrow the temporal window for the high-temporal resolution measurement.

During the pump-probe scans the intensity of the pump is also recorded before and after being transmitted through the sample using 2 photodiodes. The first photodiode is placed at the weak reflection of the Brewster window placed at the entrance of the attosecond beamline, and the second one is placed in the imaging system. Comparing both photodiode signals the influence of the SXR on the pump signal could potentially be identified. This data is not shown here because it was not conclusive in providing additional information due to the high noise contribution. There are 2 main sources of the signal fluctuations. The transmitted signal through the sample is poor when it reaches the second photodiode, generating a maximum voltage amplitude of 15 mV. In addition, the second photodiode sits on the imaging system which is a non vibrational decoupled breadboard. This last source of noise could be solved by measuring the transmitted pump signal through the sample inside the vacuum chamber where the sample sits and sharing the vibration decoupled breadboard. However, our lab is not equipped with a vacuum compatible photodiode that can detect radiation at 2$\mu$m.

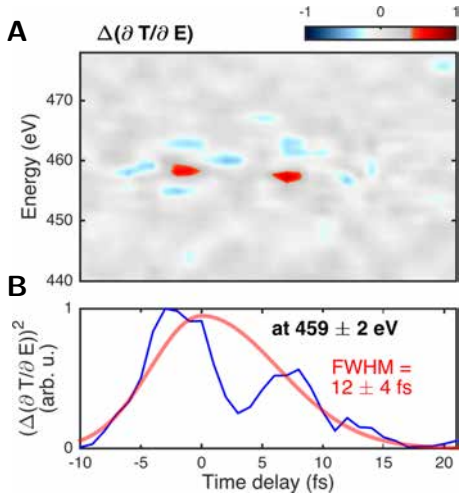


**Fig. 4.16: IR-pump envelope printed in the absorption changes.** (**A**) Spectral derivative of the transmitted transient changes with a delay step of 3 fs and an integration time of 6 min. (**B**) Integrated signal shown in (A) around the absorption edge to show a FWHM of (12 ± 4) fs.

### 4.3.3 Inter and Intra-band dynamics

To get a first impression of the possible dynamics, the Rabi frequency and Bloch oscillations are estimated for a field strength of (0.077 ± 0.008) V/Å inside the material. While such estimation is overly simplistic, it nevertheless provides a rough gauge which dynamics may dominate. The strength of intra-band charge transfer is gauged by calculating the Rabi frequency according to

$$\omega_{Rabi} = \frac{d_{cv} F_L}{\hbar} = 6.2 \cdot 10^{13} s^{-1}, \tag{4.1}$$

where $\hbar$ is the reduced Planck constant, $d_{cv} = 8.478 \cdot 10^{-30}$ C·m is the dipole moment in $TiS_2$ at the $\Gamma$ point in the Brillouin zone (taken from our DFT calculation, described below in Sec. 4.4), and $F_L$ is the electric field amplitude. Note that the Rabi frequency is only dependent on the dipole moment and the field amplitude but not on the photon energy and it entirely neglects the possibility of tunneling excitations. The strength of inter-band charge transfer can be gauged by calculating the frequency of Bloch oscillations according to

$$\omega_{Bloch} = \frac{e F_L a}{\hbar} = 4.0 \cdot 10^{14} s^{-1}, \tag{4.2}$$

where $e$ is the electron charge and a = 3.36 Å is the effective lattice constant that the impinging field probes for an incidence angle of 30 deg.

While clearly not being quantitative, the comparison between the Rabi and Bloch frequencies provide a first hint at the dynamics. Rabi frequency is smaller

than the Bloch frequency with the latter one being on a similar magnitude than the optical frequency of the pump light, $\omega_L = 1{\cdot}10^{15}\ s^{-1}$. Intra-band dynamics are expected to play a significant role and Rabi oscillations are negligible for the pump field strength.

## 4.4 Theoretical approach

In order to obtain physical insight into the underlying carrier dynamics and the link to the observed variations of the SXR absorbance (e.g. the origin of negative values in the differential absorption) theory is required. In addition to an ab-initio real-time time-dependent DFT (RT-TDDFT) calculation[201] within the adiabatic local density approximation[206] which is performed with the SALMON (Scalable Ab-initio Light-Matter simulator for Optics and Nanoscience) code package[207], to disentangle the various concurrent inter- and intra-band contributions of laser excitation, a time-dependent theoretical approach is developed by our group to describe the evolution of carriers in reciprocal space upon laser pulse excitation similar to the well-known semiconductor Bloch equations, but with the inclusion of core-level transitions by the SXR pulse. This core-state-resolved Bloch equation model (cBE, described in Sec. 4.4.2) is used to mimic the experimental conditions which we find to be accurately modelled by including the relevant three highest-occupied valence band states and two-lowest-occupied conduction band states together with the Ti-2p core states. The initial-state configuration and the relevant transition dipole matrix elements are pre-calculated using density-functional theory (DFT, described in Sec. 4.4.1)[203,206,208].

Figure 4.17 shows the result of our cBE simulation for the experimental parameters with simulated full resolution and also taking into account the spectrometer resolution of 0.6 eV.

The good qualitative match between the measurement, Fig. 4.10, and calculations, Fig. 4.17(B), is further confirmed in Fig. 4.18, which shows the differential absorption integrated over an energy interval of 5 eV where the changes are most prominent (between 457 and 462 eV).

Positive induced transmission changes are related to relative maxima on the electric field amplitude whereas negative induced transmission changes are assigned to a zero pump electric field. Zero changes refer to the transition between positive and negative changes. Validated by the good agreement between experiment and theory, the cBE model enabled us to investigate how the laser-induced carrier dynamics modifies the core-level transition and thus allows utilizing the time-resolved absorption spectrum to interpret key aspects of carrier dynamics inside the mate-

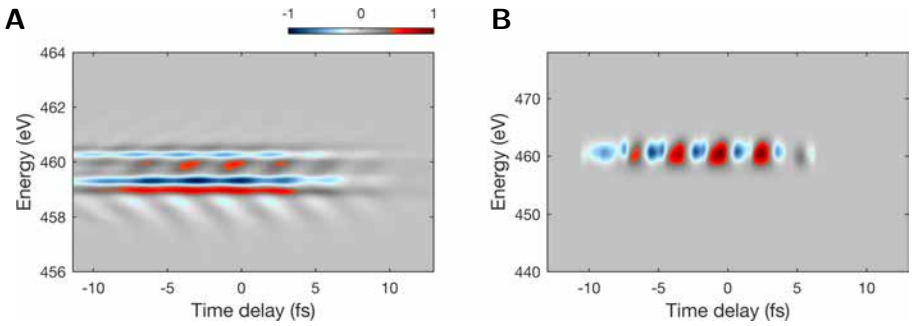


**Fig. 4.17: Calculated attosecond time-resolved XAFS.** Shown are $\Delta T/T_0$ which are calculated using a time-dependent cBE model with DFT. The DFT is used to determine the initial state configuration and the transition dipole matrix. (**A**) shows the full resolution of the simulations and (**B**) accounts for experimental spectral resolution. The model reproduces the measured oscillations as well as its positive and negative differentials.

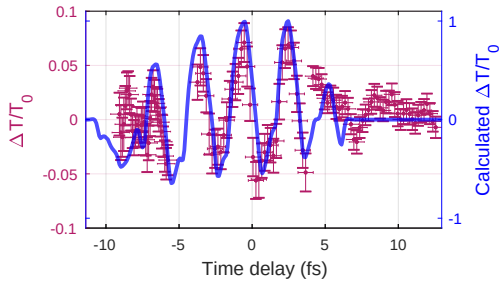


**Fig. 4.18: Calculated attosecond time-resolved XAFS.** Compares the pump-induced modifications of the SXR optical density integrated over a 5 eV energy interval (from 461.6 eV to 456.9 eV) as observed in the experiment (red) with the predictions obtained in the cBE model (blue) and shows good qualitative agreement.

rial.

In particular, the cBE model enables us to investigate the different contributions of the electron dynamics by selectively excluding the dispersion of the bands to study solely inter-band transitions at a specific k-space position. The time-resolved induced spectral changes that would be caused by the presence of the IR pump pulse by only considering inter-band transitions are shown in Fig. 4.19. These changes are directly connected to the transfer of electrons from the valence to the conduction band at a specific k-space position which results in an increase in the transmitted SXR radiation. Since a core-level transition (from Ti-2p to Ti-3d) accesses conduction band states, this leads to a decrease of the SXR absorption from Pauli blocking[204] due to the new excited DOS. Also shown in Fig. 4.19 are the corresponding temporal evolution of the respective valence excitation calculated with the cBE theory (brown) together with the valence excitation from the

RT-TDDFT calculation[201] (blue).

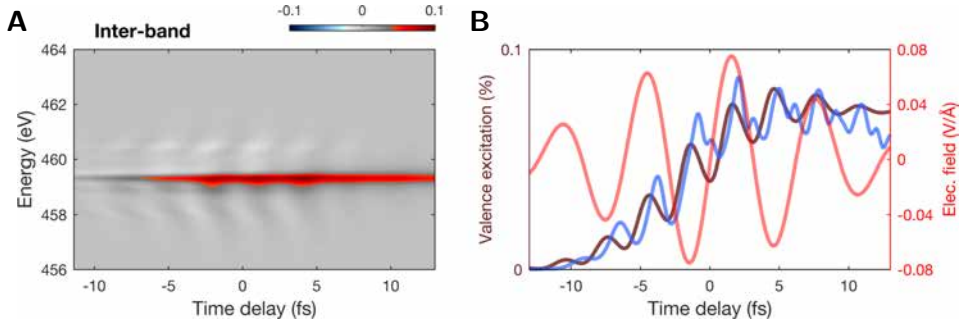


**Fig. 4.19: Inter-band transitions contributions.** (**A**) shows the calculated absorption spectrum (cBE model) considering solely inter-band carrier motion. The spectra is normalized to the maximum absolute value of the full calculation shown in Fig. 4.18(A). (**B**) quantitative prediction of the time-resolved valence excitation, obtained from the cBE (brown) and the RT-TDDFT models (blue), in relation to the pump field (red).

The signature of the population dynamics, which is dominated by inter-band transitions, is an oscillation only towards positive values (red) in the absorption spectrum and at twice the excitation laser frequency. The absence of negative-valued (blue) excursions in the calculated absorption spectrum already hints at the importance of intra-band transitions. In addition the overall effect of only considering inter-band transitions is 10% of the total changes caused by allowing inter- and intra-band transitions. This quantifies the idea that the main electron dynamics are governed by intra-band transitions over the inter-band transitions. In other words, the electron dynamics induced by the pump pulse are mainly electric-field-driven instead of photo-driven.

Within this scenario, we can further disentangle the different signatures of resonant and off-resonant contributions. While resonant inter-band transitions, e.g. at the $\Gamma$ point (0.23 eV), directly promote electrons from the valence to the conduction band, off-resonant inter-band transitions are dominated by tunneling-type excitations. Remarkably, we find that the optical response is governed by a non-resonant transition scenario at the crossover between semiconductor and a dielectric material behaviour[209], ie. at the k positions where the direct bandgap is larger. The large spectral bandwidth of the excitation pulse accesses a much higher DOS in the valence bands compared to the much smaller DOS of transitions originating close to the Fermi level.

Additionally, we find that the excursion of the carriers in the reciprocal space depends on both the field strength and the wavelength of the excitation laser. Most importantly, the absorption spectrum, shown in Fig. 4.17, oscillates also at

twice the excitation laser frequency and exhibits excursions to both positive and negative values. This oscillation is a complex interplay of secondary contributions from Pauli blocking, due to carriers that are promoted from the valence to the conduction bands and preclude the excitation of core electrons, and a dominant accumulated time-dependent phase of core electrons excited into the conduction band. The accumulated time-dependent phase depends on the initial k-space position at which the core electron is promoted into the conduction band, and the light-field driven electron motion in the dispersive energy bands, resembling the dynamical Stark shift in the time domain description of atomic experiments[210]. Based on our investigation, we caution that the 2 oscillations are ubiquitous to secondary tunneling excitations and to largely intra-band transitions.

In Fig. 4.20 the dipole response of the system is shown at three different time delays between the attosecond X-ray pulse and the IR pulse, calculated with our cBE model (see below, Sec. 4.4.2). A time-dependent phase builds up for time delays in which the X-rays arrive to the system before or around the same time as the IR pulse, however this effect vanishes when the X-rays arrives after the IR pulse and after the decay of the core hole (around 3.0 fs[105]). This effect is a consequence of the energy change due to the intra-band dynamics. Note that the acquired laser-induced phase depends on both the intensity and wavelength of the IR pulse as well as the energy dispersion of the probed band. By studying the dipole response of the system at different time delays, we observe that the profile is different, but indeed a time-dependent dephasing builds up.

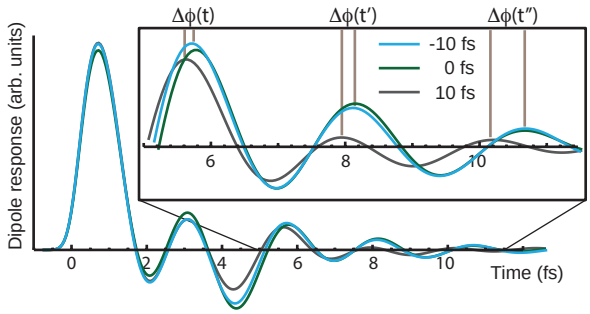


**Fig. 4.20: Dipole response of the system.** Intra-band dynamics modify the energy of the core-hole state created by the attosecond X-ray pulse. After X-ray excitation at three different time delays with respect to the IR pulse, the induced dipole response in time, Re[$\mu(t)\cdot\cos(\omega_x t)$], is represented, where $\mu(t)$ is the time-dependent dipole response of the system and $\omega_x$ is the SXR central frequency counting for the slow variant approximation. This approximation neglects the fast oscillating contributions that oscillate at the SXR frequency.

An important aspect to interpret time resolved absorption spectra is the significant modification of the absorption line shape of the core-level transition due

to the rapidly oscillating optical excitation field acting on the final state wavefunction. Figure 4.21(B) shows, in analogy with the atomic case[211], that pump-laser dressing of the core-state significantly modifies the field-free Lorentzian absorption line-shape resulting in the laser-dressed Fano-type line-shape[211,212]. In the condensed phase however, such modification of the line-shape is significantly more complex for the condensed phase since the Fano-phase is a function of reciprocal space, as shown in Figs. 4.21(A) and 4.21(B). Due to the spectrograph's limited resolution of 0.6 eV, we are not able to directly resolve the sidebands and the subtle modifications of the absorption spectrum, but the main features, such as the positive and negative-valued excursions oscillating at twice the laser frequency, are nevertheless clearly evident in Fig. 4.17(B).

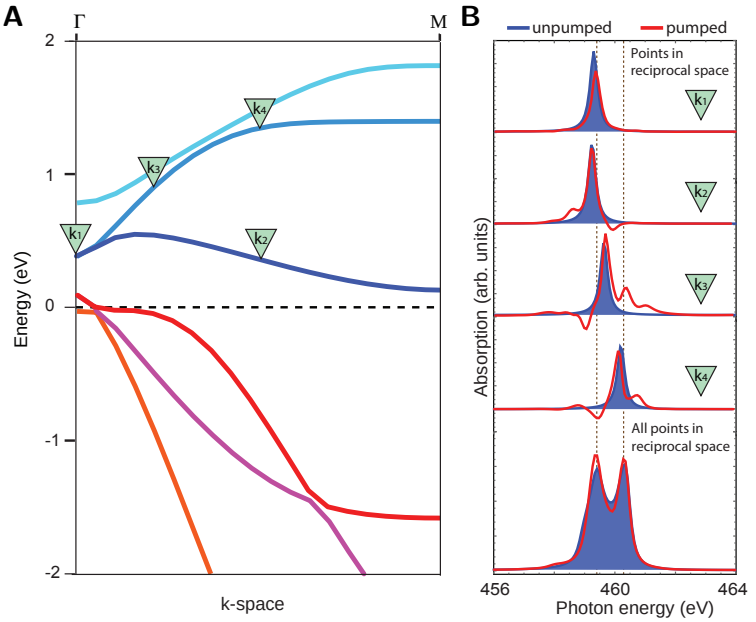


**Fig. 4.21: Induced absorption line-shapes.** (**A**) shows the band energy dispersion along the $\Gamma$ and M points and (**B**) associated soft X-ray absorption lines at four points of the reciprocal space. The unpumped case is shown in blue and the red curves show how the presence of the IR pump pulse alters the absorption line-shapes from the unperturbed Lorentz-profile to a Fano-type profile.

Having investigated the predominant contributions of carrier dynamics to the absorption spectrum, we exploit the element-specificity of the attosecond SXR pulse[213] to examine the spatio-temporal flow of carriers inside the material. Here, we use the fact that Ti-2p core-level transitions exclusively probe Ti-3d character conduction band states, while the valence band is predominately composed of S-character states. On the basis of the good qualitative agreement between theory and experiment, this permitted leveraging the theoretical model to visualize the oscillation of charge within the unit cell between the Ti and S atoms of the material.

Figure 4.21 shows the time-dependent charge density oscillations and the DOS for two field strengths computed using both the cBE and RT-TDDFT codes (code details are shown in Secs. 4.4.2 and 4.4.3, respectively).

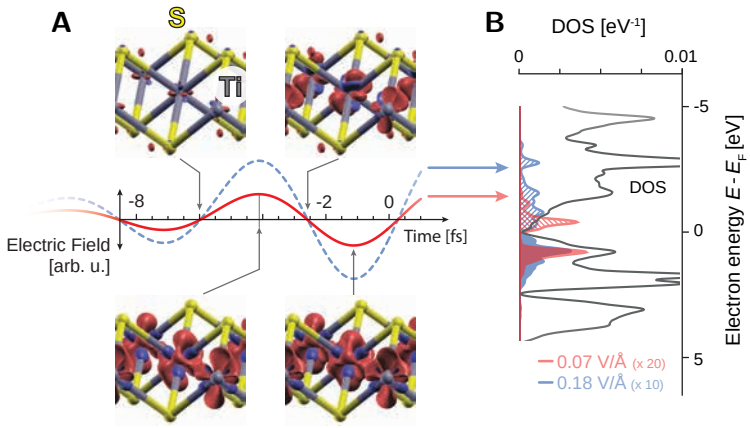


**Fig. 4.22: Spatio-temporal dynamics of the electron density distribution inside the unit cell.** (**A**) At different moments within the electric field oscillation, the difference of electron density is displayed with respect to the ground state (4 panels showing the carrier density displacement within the unit cell). Increased and decreased density are shown in red and blue, respectively. The time-dependent difference shows a $2\omega_L$ population increase at Ti-3d orbitals. (**B**) DOS and light-induced occupation: RT-TDDFT computations observe the transition from a distribution of occupied states within the DOS split in accordance with the pump pulse spectrum ($\approx$ 0.5 - 1 eV) for the field amplitude of 0.07 V/Å (occupied DOS in shaded red, unoccupied DOS in red) towards a more distributed excitation profile extending both into higher and lower energetic intervals of the valence and conduction bands already for a peak field of 0.18 V/Å (occupied DOS in shaded blue, unoccupied DOS in blue).

Depicted is the change of the electron density distribution that displays only a change with respect to the ground state (unpumped case), with red (blue) isosurfaces indicating increasing (decreasing) density; the anisotropic distribution of this charge-density difference reflects the hybridization between Ti-3d and S-3p states. A clear charge depletion is observed along the bond and we find an associated increase with electronic density on the Ti state with d-character. The charge re-distribution occurs within a femtosecond over a distance nearing half the distance between Ti and S atoms of 2.4 Å with a frequency commensurate with the half-cycle period of the IR pump laser. The charge re-distribution increases in distance with the increasing field amplitude of the IR laser pulse, thus visualizing the IR field-driven motion of charged carriers within the unit cell.

Interestingly, according to the RT-TDDFT computations at the low field amplitude of 0.07 V/Å, used in this study, the excitation profile of carriers promoted

into the conduction band DOS mimics the pump pulse' photon energy spectrum with transitions originating from valence band states just below the Fermi energy into conduction band states approx. 0.5 - 1 eV above the Fermi energy. Clearly discernible is also an energy gap between the depopulated valence and populated conduction band states (shaded red and red distribution in Fig. 4.22(B), respectively). While the temporal evolution of the electronic transitions confined to the field crests of the pump light field resemble tunneling behaviour, the observed confinement of occupied states spaced by one photon energy of the pump light spectrum highlight that the observed effects indeed play out in the weak field regime which is in accordance with a Keldysh parameter of 2.5[214,215]. For pump pulse amplitudes 2.5 times higher (i.e. 0.18 V/Å), carriers are promoted into more energetic conduction band states and, surprisingly, also to states closer to the Fermi level, that remain unpopulated for low field amplitudes. This significant redistribution of DOS (blue and blue dashed population distribution) further highlights the concomitant occurrence of inter- and intra-band transitions even at modest field strengths.

### 4.4.1 Density-functional theory (DFT) calculations of the electronic band structure and dipole matrix elements

The electronic structure of the system is computed from first principles in the framework of density-functional theory[161], as implemented in the all-electron full-potential code exciting[193]. This computer package is based on the linearised augmented plane wave plus local orbital (LAPW+LO) method and is able to accurately treat crystal structure by applying periodic boundary conditions. The Kohn-Sham equations[192] are solved on a 10x10x8 k-grid, using a plane-wave cutoff of $G_{max}$ = 5.5/Bohr for the basis set, where $G_{max}$ is the maximum of the reciprocal lattice vectors $G$. Muffin-tin spheres of radius 1.45 Bohr and 2.00 Bohr are adopted for sulfur and titanium, respectively. The generalized gradient approximation is used for the exchange-correlation potential, employing the Perdew-Burke-Ernzerhof parametrization[201]. Experimental lattice parameters a = 6.34 Bohr and c = 10.77 Bohr (a = 3.36 Å and c = 5.70 Å) are used to model bulk $TiS_2$. Transition-dipole moments for both valence- and the core-conduction transitions are calculated from LAPW within the independent-particle approximation[203].

The ground electron density is calculated as

$$\rho(r) = \frac{1}{N_k} \sum_{b,k} |u_{bk}(r)|^2 \tag{4.3}$$

where the function $u_{bk}$ is the Bloch orbitals that have the lattice periodicity for each band index $b$ and Bloch wavevector $k$. The time-dependent electron density

used in Fig. 4.22 are calculated by first propagating the system with the cBE model, extracting the occupation number for the different Bloch functions, and computing again the electron density of the system.

### 4.4.2 Core-resolved Bloch Equation Theory (cBE)

In order to describe the dynamics of charge carriers of the system with the additional possibility to investigate the individual contributions to the absorption signal, a time-dependent theoretical approach is developed to account both for the IR laser pulse excitation and for the SXR pulse excitation inspired in a previous time-dependent Schrödinger equation (TDSE) for molecular inner-shell dynamics[216] (Eq.(4.4)). The theoretical model is based on limiting the many-body wavefunction to those electronic states that contribute to the electron dynamics. Core-hole states (m) are separated from those states that involve holes and particles around the Fermi level shells ($\lambda$):

$$|\Phi(r,t)\rangle = \sum_m \int dk^3 a_m(k,t)|k,m\rangle + \sum_\lambda \int dk^3 a_\lambda(k,t)|k,\lambda\rangle \tag{4.4}$$

where the wavefunction is expanded in a Bloch function basis, and $a_m$ are the corresponding time-dependent amplitudes. Now, by including this ansatz in the TDSE, a couple of differential equations for the amplitudes are obtained, also known as equations of motion (EOMs). From the EOMs it is possible to derive the equations of evolution in a density matrix formalism and obtain a model similar to the well-known Bloch equations for semiconductors[217] but in this case we explicitly account for core-hole states. The cBE model allows then the calculation of the electron carrier dynamics in the reciprocal space accounting both for intra-band and inter-band couplings. After X-ray excitation, core-hole states are coupled with the IR laser pulse, and the X-ray response of the system is calculated beyond the linear behaviour. The attosecond absorption spectra displayed in Fig. 4.17(B) are calculated using the response function[218];

$$S(\omega) = 2 \cdot Im[\mu(\omega)E^*(\omega)] \tag{4.5}$$

related to the cross section as $\sigma(\omega) = 4\pi\alpha\omega S(\omega)/|E(\omega)|^2$ where $\alpha$ is the fine-structure constant, E is the Fourier transform of the electric field and the Fourier transform of the dipole response of the system $\mu$(t) is given by

$$\mu(t) = q\sum_{\lambda m} \int dk^3 \rho_{m\lambda}(k,t) d_{m\lambda}(k) + c.c. \tag{4.6}$$

where $q$ is the electron charge and $\rho_{m\lambda}$ is the electron density matrix at each band. The dipole matrix $d_{m\lambda}$ involves dipole transitions between the core orbitals

and unoccupied orbitals near the Fermi level. Experimentally, the X-ray absorption spectral changes are located around 460 eV, in the pre-edge region. In order to model this region, the three highest occupied valence bands and the two lowest unoccupied conduction bands are included in the cBE model.

The changes of the line-shape profile are related to the energy modifications of the core-hole state after SXR excitation under the presence of the IR pulse. This is easy to understand in the time-dependent dipole formalism that is developed for describing the atto-tr-XAFS lineshape profiles of Fano resonances in atomic systems[210]. The extension of this formalism to solid systems can be done by writing the dipole response of the system as the sum of all dipole transitions in the reciprocal space

$$\begin{aligned}\mu(t) \propto \int dK^3 \left[ b(K,t) e^{-i\int_{t_0}^{t} dt'(E_c(K+A(t'))-E_{ch}(K+A(t'))-i\Gamma_{ch}/2)} + c.c. \right] = \\ \int dK^3 \left[ b(K,t) e^{-i(E_c(K)-E_{ch}(K)-i\Gamma_{ch}/2)(t-t_0)-i\phi(t,t_0,K)} + c.c. \right]\end{aligned} \tag{4.7}$$

where $E_c$ stands for the energy in the conduction band, and $E_{ch}$ stands for the energy of the core hole state. The vector potential $A(t)$ is related to the electric field applied to the unit cell by $E(t) = -\partial A/\partial t$. K is a change of variable $K = k - A(t)$ and $b(K,t)$ is the re-defined time-dependent amplitudes. Note that the Keldysh transformation is used, in which the quasi-continuum states are replaced by the corresponding ones in the dressed picture when an electric field is present. The vector potential $A(t)$ is related to the electric field applied to the unit cell by $E(t) =$ - $\partial A/\partial t$. $\Gamma_{ch}$ stands for the decay rate of the core hole state. The phase is defined as

$$\phi(t,t_0,K) = -i\int_{t_0}^{t} dt' \left[ \left(E_c(K+A(t')) - E_{ch}(K)\right) - \left(E_c(K+A(t')) - E_c(K)\right) \right] \tag{4.8}$$

In general, the energy band of the core-hole state does not present strong dependence with K. In the case that the vector potential is small, we can approximate the phase in first order of perturbation theory

$$\phi(t,t_0,K) = i\int_{t_0}^{t} dt' \left[ E_c(K+A(t')) - E_c(K) \right] \approx i\int_{t_0}^{t} dt' \frac{\partial E_c(K)}{\partial K} A(t') + O(2) \tag{4.9}$$

It is a good approximation to neglect the change of the energy dispersion of the core-hole band with respect to the quasi momenta. Hence, this shows that the dipole response acquires an additional phase that is induced by the IR pulse during the core hole decay. This additional phase is known in atomic systems to influence the lineshape profile of the atto-tr-XAFS spectrum, converting Lorentzian profiles

into Fano profiles[210]. Here, the phase dependence is summed over all K space, and its effect is much more complex than in a simple atomic system.

### 4.4.3 Real-time Time-dependent Density Functional Theory (RT-TDDFT) calculation

Time-dependent density functional theory (TDDFT) has been widely used to describe electronic excitations and optical responses of isolated and extended systems at the first-principle level. Here, we employ a real-time TDDFT (RT-TDDFT) to describe electron dynamics in a single-layer $TiS_2$ crystal, solving the time-dependent Kohn-Sham equation in time domain. The RT-TDDFT has been widely used to describe electron dynamics in atoms, molecules, and solids under irradiation of intense and ultrashort laser pulses without any empirical parameters. In the present application, we consider a spatially uniform, time-dependent electric field along the 1T-$TiS_2$ crystal structure.

The time-dependent Kohn-Sham equation that describes electron dynamics in a unit cell under a pulsed electric field is given by, assuming atomic units,

$$i\frac{\partial u_{bk}(r,t)}{\partial t} = \left[-\frac{1}{2m}(p+k-A(t))^2 + V_H + V_{xc} + V_{ion}\right] u_{bk}(r,t) \qquad (4.10)$$

where $V_H$, $V_{xc}$ and $V_{ion}$ represent the Hartree, the exchange-correlation, and the electron-ion Coulomb potentials, respectively. The function $u_{bk}$ represents a time-dependent Bloch orbitals that have the lattice periodicity. The label $b$ refers to the band index and $k$ refers to the Bloch wavevector. For the electron-ion Coulomb potential, we employ norm-conserving pseudopotentials, in which the 3s-states of S atoms and the 3s,3d-states of Ti atoms are treated as valence electrons. We use the Perdew-Zunger functional in the adiabatic local density approximation (ALDA). We numerically solve the time-dependent Kohn-Sham equation by using the SALMON code[207]. The electron density in time is calculated as

$$\rho(r,t) = \frac{1}{N_k}\sum_{b,k}|u_{bk}(r,t)|^2 \qquad (4.11)$$

The excited population of Fig. 4.19(B) is calculated by taking the changes of the electron density in an integrated volume containing the Ti atoms. We investigate the spatial distribution of the electronic excitations which contributes to the $2\omega$ oscillation. For this purpose, it is convenient to separate the electronic excitations into linear and non-linear components. This non-linear component is obtained by subtracting the linear density change, which is predicated by the response to the small perturbation field, from the total electron density change.

We plot the non-linear component electron density change in Fig. 4.23. In the ground state, the top of the bonding orbit is mainly formed by the 3p orbit and has a small but not the negligible contribution from Ti(3d) $e_g$-like orbit facing the direction of S atoms. The optical excitation leads the transition to the $t_{2g}$-like orbits corresponding to the red region. This region is orientating in the direction apart from the S atoms to avoid the coulomb repulsing from the $S^{2-}$. At the same time, due to the decrease of the electron from the $e_g$-orbit contained in the bonding orbit, the blue region appears in Fig. 4.23(B).

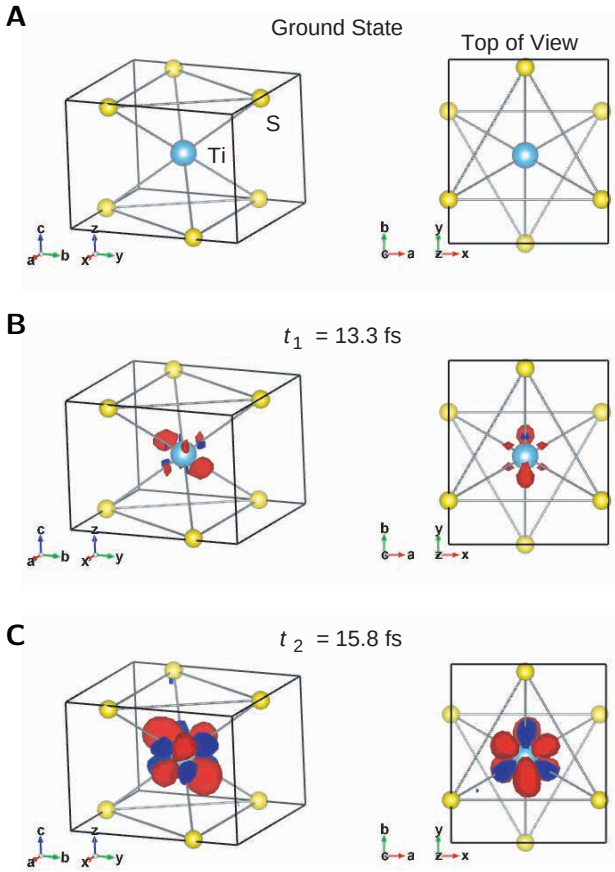


**Fig. 4.23: Non-linear component of the TDDFT electron density distribution.** Shown are the ground state (**A**) and charge profile at two characteristic times $t_1$ (**B**) and $t_2$ (**C**). This times correspond to the dip and peak position of the valence excitation in Fig. 4.19(B), respectively. The red- and blue- coloured regions indicate the increase and decrease of the electron density, respectively.

## 4.5 Investigation of spectral pump absorption femtosecond dynamics in $TiS_2$

Due to the broad bandwidth of the pump pulse, shown in Fig. 1.1, for the time-resolved attosecond measurement, we undertake an investigation into the wavelength dependence of electronic excitation and aim at identifying electron dynamics inside the band structure. Moreover, in order to also establish an adequate pump field strength well below the damage threshold, we undertake time-resolved measurements of the IR absorption for a variety of pump fluences.

For our investigation on how excitation depends on pump wavelength, the measurements are carried out with a different setup which provides spectrally tunable, and more narrowband, pump pulses in addition to probe pulses at a central wavelength of 800 nm. The pump pulse's energy tunability with a fairly narrow spectral bandwidth of less than 40 meV, allows to energetically select the different electronic transitions from the valence to the conduction band. The pump pulses can be tuned to wavelengths from 1.5 $\mu$m to 2.1 $\mu$m (see Fig. 4.24) which are generated in a collinear optical parametric amplification (OPA) scheme, seeded with a sub-40-fs, 800 nm output from a Ti:Sapphire laser. Overall, 4.7 W at 5 kHz are available from the Ti:Sapphire laser system from which a part of the energy pulse is used. The OPA crystal's phase matching angle can be tuned to change the central wavelength of the amplified idler or signal. The OPA's signal can cover wavelengths up to 1500 nm whereas the idler reaches wavelengths above 1550 nm. Both, the 800-nm seed and the idler have p-polarization whereas the signal is s-polarized. The OPA output yields pulse durations that are less than 80 fs and a maximum power of 40 mW at the sample is used.

The sample is positioned perpendicular to the propagation direction of the 800 nm probe beam and the 1.5 $\mu$m to 2.1 $\mu$m pump beam is incident onto the sample at an external angle of 17 degrees. In the sample plane the probe beam has a measured beam size of 40 $\mu$m at FWHM and the pump beam is at least twice as large with beam sizes of 88 $\mu$m at FWHM for all wavelength expect for 1.5 $\mu$m which is 130 $\mu$m at FWHM. Pump fluences between 9 mJ/cm$^2$ and 11 mJ/cm$^2$ are used.

The sample holder which is used in the experiments is shown in Fig. 4.25. It consists of a 200 nm $TiS_2$ sample (mounted identically to the one displayed in Fig. 4.3), a 100 nm $VO_2$ sample on a 100 nm $Si_3N_4$ membrane and a nickel disc with 100 $\mu$m aperture.

The bare nickel disc with 100 $\mu$m diameter hole is used to ensure that both pump and probe beams overlap thereby ensuring accurate probing of the excitation

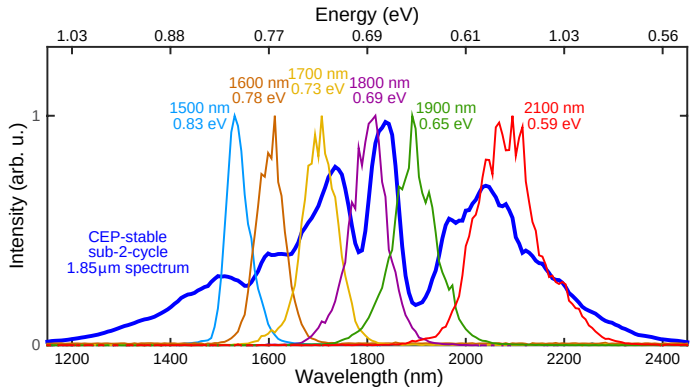


**Fig. 4.24: Spectral coverage of the narrow-band OPA.** Shown is the idler wavelengths accessible with the 800-nm-pumped OPA system together with accessible signal wavelength. These spectra are overlaid with the CEP stable sub-2-cycle pump spectrum (thick blue curve).

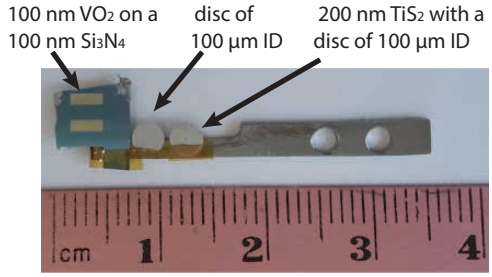


**Fig. 4.25: Sample assembly for the 1.5 to 2.1 $\mu$m pump and 800 nm probe transient absorption experiments.** Visible in the picture (from left to right) is a $VO_2$ crystal with a thickness of 100 nm on 100 nm $Si_3N_4$ membrane, a sole nickel disc with 100 $\mu$m aperture, and a 200 nm thin $TiS_2$ sample situated on top of a TEM grid with 90 $\mu$m square-hole aperture and a 100 $\mu$m diameter nickel disc which defines the probed area.

volume inside the material. The 800 nm probe beam has a fixed beam path and is focused by a lens with 150 mm focal length to the plane where the sample holder is placed. The disc's centre orifice is moved towards the centre of the probe beam. Afterwards the pump beam is positioned to maximize its transmission through the disc's hole. After determining spatial overlap, the temporal overlap is adjusted. To this end, the $VO_2$ sample is used since it exhibits a strong and well known transient signal as response to pumping at 1.7 $\mu$m wavelength. The pump fluence is set to $(11.8 \pm 0.3)$ mJ/cm$^2$ and the beam is chopped at a frequency of 413 Hz to detect the response with a photodiode and a lock-in amplifier. This scheme is used for all 800 nm probe measurements presented here.

Figure 4.26 shows that the transmitted signal through $VO_2$ decreased for

positive delays, i.e. after the pump pulse. Subtracting the exponential decay fit from the measured ring-down signal, the 5.7 THz phonon can be observed in $VO_2$ [219], which permits placing an upper limit of 87.7 fs on the cross-correlation signal. The maximum signal response is chosen as zero delay marker.

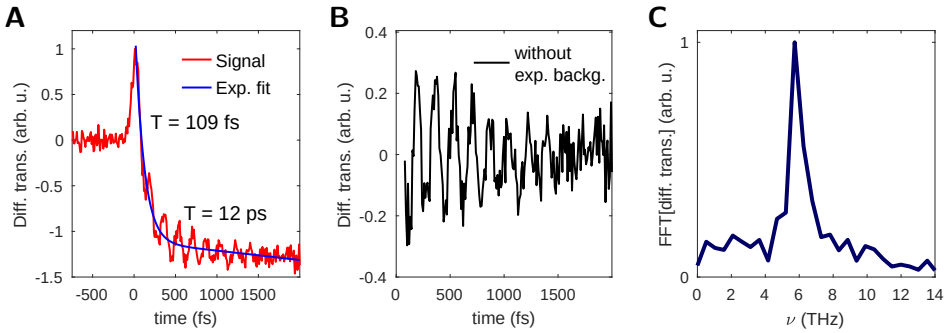


**Fig. 4.26: Transient absorption in $VO_2$ as reference measurement.** (**A**) shows the transmission changes as function of pump probe delay (red curve). It exhibits an ultrafast decay which can be fitted with a bi-exponential decay (blue curve) with decay times of 109 fs and 12 ps. (**B**) Phonon oscillations are observed 80 fs after the pump pulse maximum and a Fourier Transform (**C**) reveals the dominant phonon mode at (5.73 ± 0.05) THz.

Having ensured spatial-temporal overlap of the pump and probe pulses using $VO_2$, the $TiS_2$ sample is investigated. Figure 4.27 shows the change in absorption for a range of pump wavelengths ranging from 1.5 $\mu$m to 2.1 $\mu$m in order to mimic the 2-cycle, 1.85 $\mu$m pulse's spectrum.

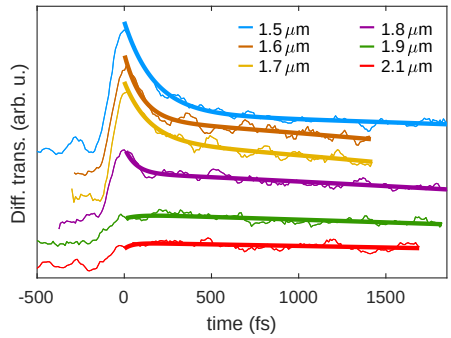


**Fig. 4.27: Transient optical absorption in $TiS_2$.** Shown are time-resolved transmission measurements for a range of wavelengths between 1.5 and 2.1 $\mu$m and pump fluence between 9 to 11 mJ/cm$^2$. The measurements are overlaid with bi-exponential fits of the decay curves. We find that pump wavelengths lower than 1.85 $\mu$m exhibit a fast rising transmission change that decays with an average time constant of (110 ± 20) fs. All pump wavelengths display a longer time decay of (14 ± 4) ps (on average).

The time-resolved transmission for wavelengths ranging from 1.5 to 2.1 $\mu$m uses fluences ranging between (9.0 $\pm$ 0.2) mJ/cm$^2$ and (11.0 $\pm$ 0.4) mJ/cm$^2$. Increasing the fluence further, e.g. to (11.8 $\pm$ 0.3) mJ/cm$^2$ at a wavelength of 1.7 $\mu$m, results in irreversible behaviour and, thus, indicates the damage threshold of the material.

Overall, we observe a wavelength-dependent change in transmission. We find that wavelengths between 1.5 and 1.9 $\mu$m result in a fast rise of transmission followed by an initial ultrafast electronic decay with an average time constant of (110 $\pm$ 20) fs and a later, slower, decay with a time constant of (14 $\pm$ 4) ps. Wavelengths of 1.9 $\mu$m and longer exhibits a markedly different behaviour since the initial ultrafast recovery entirely disappears. The recovery of all wavelengths will be finally limited by transverse thermal diffusion. The difference in dynamics could come from low photon energies exciting electrons in the conduction band, whereas the higher photon energies also excite electrons across the band gap.

## 4.6 Conclusion

Attosecond SXR pulses are ideally suited to harvest the full potential of XAFS to interrogate charge dynamics in real time, thereby providing unprecedented insight into the inter- and intra-band motion of carriers inside a material. We observe that light-driven electron dynamics in $TiS_2$ close to the Fermi level lead to an unexpected modified X-ray-absorption line shape with an increase of absorption in the core-level photo-electron excitation to the conduction band.

Important for the interpretation of attosecond transient XAFS measurements, even for small pump-field strengths, are the inclusion of pump-field induced line-shape modifications from Lorentzian to Fano-type due to an acquired dipole phase response of the absorbed SXR radiation induced by the consecutive arrival of the IR pump, which demonstrates the realization that field-driven intra-band dynamics appear dominantly over inter-band dynamics.

The induced dipole phase changes accumulate during the lifetime of the core-hole excitation. Using SXR radiation brings access to core-level electron excitations which have femtosecond core-hole decays[105] allowing sub-cycle laser-induced electron dynamics to be resolved.

Moreover, the element specificity of attoXAFS permits, in combination with theory, to visualize the flow of charge amongst the atoms inside the unit cell in real time. Such precise knowledge may be the key to enable tuning material properties through intercalation in which the distance to the host atoms may be tailored to the

dynamic properties of the wavefunction's excursion. Furthermore, the combined spatio-temporal capabilities of atto-tr-XAFS may prove decisive to investigate the correlated motion of carriers in quantum materials and to re-examine long-standing questions for phase-transitions[220,221] and superconductivity in layered materials[221].

# 5 Summary and Outlook

In this thesis we make use of the demonstration of the generation of isolated attosecond pulses in the soft X-ray regime covering the entire water window with pulse durations shorter than 300 as. Such a source is used to explore its own development, the spectroscopic capabilities of the pulses and the spectroscopic differences with existing X-ray sources as well as to exploit the potential of the provided extraordinary temporal resolution. These capabilities lead to three main experimental findings presented in this thesis that provide insights into chemical and physical processes that occur on the attosecond timescale.

In Chap. 2, the macroscopic characteristics of a controlled tunable HHG source in the SXR regime are determined which is vital for the development of attosecond sources with spectral flexibility. We generate attosecond SXR radiation that is tuned to around 150 eV across the water window by changing either the $z$ position of the HHG target with respect to the focal plane of the driving laser by 500 $\mu$m or the maximum pressure at the interaction region by 3.5 bar. Simulations subsequently correlated both macroscopic changes, pressure and $z$ position, to a change in phase matching between the driving laser pulse and the generated HHG radiation that is mainly caused by a change in the ionisation fraction. These phase matching changes are comparable to a CEP change of the driving laser field.

Accurately measuring the pressure distribution along the HHG target and the beam propagating wavefront enables an in-depth study into the phase matching conditions of our SXR laser pulse. One method to measure the pressure distribution inside the target is through interferometry by using a transparent HHG target. The transparency could be provided by an acrylic tubing that could be drilled with the laser directly. However, the pressure distribution will still have a large uncertainty since small fluctuations on the geometry, especially on the hole apertures, can lead to a significant discrepancy of the pressure distribution used in the experiment. Another parameter that significantly influences the phase matching conditions is the aperture of the iris positioned at the driving laser beam path 2 meters before the HHG target. This aperture controls both the maximum energy of the driving laser on target and the beam profile of the driving laser that propagates across the interaction region. By installing a controlled and reproducible variation of the

aperture, one could establish a relationship between the pulse energy and beam size as a function of the aperture, which could subsequently related to the spectrum of the generated attosecond pulse. Consequently, our beamline provides capabilities to measure the SXR spectral beam profile as a function of any phase matching input parameter. Such capabilities will enable future investigations into experimentally determining the cutoff energy that could be realistically reached.

In Chap. 3 the attosecond SXR source is used in an X-ray absorption spectroscopy technique, XAFS. Our XAFS studies enabled the simultaneous probing of EXAFS and XANES in graphite providing element specificity and orbital sensitivity with identification of the $\sigma^*$ and $\pi^*$ orbitals in synchronicity with the material's four characteristic bonding distances. This illustrates the potential capability of correlating electron dynamics with structural dynamics with attosecond resolution being able to resolve charge migration, electron-phonon coupling and structural transitions. Our XAFS investigations also revealed spectral changes in graphite and $TiS_2$ as a consequence of the shorter attosecond pulse relative to a picosecond pulse that are typically used in synchrotron facilities. These differences are potentially related to induced electron and vibrational dynamics due to the synchrotron long pulse duration. An extended theory is still required to link AES, TEY and XAFS using synchrotron radiation with attoXAFS to decouple the different electron dynamics involved on each of the measurements. This study could point out the limitations and advantages of either using synchrotron radiation or attosecond pulses.

In Chap. 4, the attosecond pulses are employed with their full potential of XAFS to interrogate charge dynamics with unprecedented temporal resolution inside a compound quasi-2D material, semimetal $TiS_2$. We observed that the shape of the X-ray absorption line changes from a Lorentzian distribution to a Fano-type distribution oscillating with twice the pump electric field frequency, and appears due to an acquired dipole phase response induced by the consecutive arrival of the IR pump. This demonstrates that field-driven intra-band dynamics appear dominantly over inter-band dynamics. We have successfully resolved the sub-cycle laser-induced electron dynamics due to the fast decay of the core-level electron excitation within a few femtoseconds[105]. SXR radiation also provides element specificity of attoXAFS which permits, in combination with theory, the visualisation of the flow of charge amongst the atoms inside the unit cell in real time. The combined spatio-temporal capabilities of atto-tr-XAFS may prove decisive in the investigation of the correlated motion of carriers in quantum materials such as phase-transitions[220,221] and superconductors[221].

Future work utilizing the high-resolution capabilities of our attosecond X-ray

beamline could include the combination of the simultaneously probing of electrical and structural conformation in graphite via atto-tr-XAFS. This will permit the in-situ identification of electron and structural couplings like electron-phonon coupling. Inducing electron excitations would lead to an initial distortion of the DOS expected to differ the pumping photon energy between the valence and conduction bands[222]. The atto-tr-XAFS spectra is expected to show spectral differences at the absorption edge that also differ the pumping photon energy. Hence, the higher the pump photon energy, the easier to spectrally resolve the induced dynamics. Following this requirement, it would be preferable to pump the graphite sample with a 800 nm pump pulse instead of a 1.85 $\mu$m pulse. Chap. 1 details two experimental setups with either a CEP-stable 800 nm pump to probe sub-cycle dynamics or a 800 nm pump with a fine tuned fluence to study the graphite response at different pumping intensities. It is worth noticing that in-plane optical excitations promotes electron density close to the Fermi level by a $\pi \rightarrow \pi^*$ state transitions[117]. However, in-plane SXR radiation accesses the 1s $\rightarrow \sigma^*$ transition instead of 1s $\rightarrow \pi^*$. Tilting the plane of the same to 45 deg. with respect to the SXR linear p-polarisation would still allow the 800 nm pump pulse (either in-plane or at 45 deg. out of plane) to excite electrons from $\pi$ to $\pi^*$ and the SXR radiation would be able to access the induced dynamics through the 1s $\rightarrow \pi^*$ transition.

In addition, by monitoring the transmitted IR spectrum, one could infer the effects of the attosecond SXR radiation on the energy levels close to the Fermi level. For example, shift of the energy bands due to the core-hole relaxation and Auger electron emission could be investigated.

In summary, this thesis has demonstrated unprecendented capabilities of attosecond pulses in the soft X-ray regime used for X-ray absorption spectroscopy measurements to resolve electron dynamics close to the Fermi level with element specificity.

# Abbreviations

| | |
|---|---|
| **AES** | **A**guer **E**lectron **S**pectroscopy |
| **AFM** | **A**tomic **F**orce **M**icroscopy |
| **atto-tr-XAFS** | **a**ttosecond **tr**ansient **X**-ray **A**bsorption **F**ine **S**tructure |
| **BBO** | **B**eta **B**arium B**o**rate |
| **BiBO** | **Bi**smuth **Bo**rate |
| **BSE** | **B**ethe-**S**alpeter **E**quation |
| **cBE** | **C**ore-resolved **B**loch **E**quation Theory |
| **CEP** | **C**arrier-to-**E**nvelope **P**hase |
| **CVT** | **C**hemical **V**apor **T**ransport |
| **DFG** | **D**ifferential **F**requency **G**eneration |
| **DFT** | **D**ensity **F**untional **T**heory |
| **DOS** | **D**ensity **o**f **S**tates |
| **EOM** | **E**quations **o**f **M**otion |
| **EXAFS** | **E**xtended **X**-ray **A**bsorption **F**ine **S**tructure |
| **FT** | **F**ourier **T**ransform |
| **FWHM** | **F**ull **W**idth at **H**alf **M**aximum |
| **GVD** | **G**roup **V**elocity **D**ispersion |
| **HCF** | **H**ollow-**C**ore **F**ibre |
| **HHG** | **H**igh **H**armonic **G**eneration |
| **ICP** | **I**nductively **C**oupled **P**lasma |
| **ID** | **I**nner **D**iameter |
| **IR** | **I**nfra**r**ed |
| **LAPW** | **L**inearised **A**ugmented **P**lane **W**ave |
| **LDA** | **L**ocal **D**ensity **A**pproximation |
| **LO** | **L**ocal **O**rbital |
| **LUMO** | **L**owest **U**noccupied **M**olecular **O**rbital |
| **NEXAFS** | **N**ear **E**dge **X**-ray **A**bsorption **F**ine **S**tructure |
| **OD** | **O**ter **D**iameter |
| **OPA** | **O**ptical **P**arameteric **A**amplifier |
| **RT-TDDFT** | **R**eal-**T**ime **T**ime-**D**ependent **D**ensity **F**unctional **T**heory |
| **SALMON** | **S**calable **A**b-initio **L**ight-**M**atter Simulator for **O**ptics and **N**anoscience |
| **SFG** | **S**um **F**requency **G**eneration |
| **SHG** | **S**econd **H**armonic **G**eneration |

| | |
|---|---|
| **SNR** | **S**ignal to **N**oise **R**atio |
| **SXR** | **S**oft **X**-**r**ay |
| **TDSE** | **T**ime-**D**ependent **S**chrödinger **E**quation |
| **TEM** | **T**ransmission **E**lectron **M**icroscopy |
| **TEY** | **T**otal **E**lectron **Y**ield |
| **UHV** | **U**ltra **H**igh **V**acuum |
| **UVFS** | **U**ltra**v**iolet **F**used**s**ilica |
| **XAFS** | **X**-ray **A**bsorption **F**ine **S**tructure |
| **XANES** | **X**-ray **A**bsorption **N**ear **E**dge **S**tructure |
| **XFEL** | **X**-ray **F**ree **E**lectron **L**aser |
| **XPS** | **X**-ray **P**hotoelectron **S**pectroscopy |
| **XRPD** | **X**-**r**ay **P**owder **D**iffraction |
| **XUV** | E**x**treme **U**ltra**v**iolet |

# Author's contributions

The driving laser and the beamline that provides sub-300 as SXR pulses were developed by Dr. Seth L. Cousin, Dr. Francisco Silva, Dr. Stephan M. Teichmann and Dr. Michael Hemmer. The SFA simulations in Chap. 2 as well as the dipole contribution to phase matching calculations were carried out by the author with code written by Dr. Dane R. Austin. The simulations that include spatial propagating effects were provided by Dr. Arnaud Couairon.

The attoXAFS measurements on graphite presented in Chap. 3 were acquired by the author supported by Irina Pi who also contributed in the data analysis together with the author, Dr. Iker León (IL), Prof. Antonio Picón (AP), Dr. Themistoklis P. H. Sidiropoulos (TPHS) and Dr. Dooshaye Moonshiram (DM). DM extracted the bond-distances of graphite by modelling EXAFS data. Peter Schmidt (PS) provided the sample supported by the author. The DOS calculations using a DFT core BAND were performed by TPHS who also provided Fig. 3.5. Prof. Jens Biegert (JB) provided Fig. 3.7. AP and DM provided Fig. 3.8. The experiments implemented on XAFS, AES and TEY in the synchrotron were acquired by the author supported by TPHS, JB, Dr. Azzedine Bendounan and Biplob Nandy. The data analysis was done by the author supported by TPHS, AP, Dr. Fausto Sirotti and Prof. John J. Rehr. The samples were provided by Samuel Mañas-Valero (SM) and Dr. Thomas Danz (TD).

The atto-tr-XAFS measurements shown in Chap. 4 were taken by the author supported by IL and Nicola Di Palo. Dr. Caterina Cocchi and Prof. Claudia Draxl applied DFT theory and the BSE to calculated band structure and relevant dipole moments of $TiS_2$ and partially contributed in Fig. 4.1. A.P. developed the cBE theory and provided Figs. 4.20 and 4.21. JB implemented Fig. 4.4. SM described the sample growth and provided Fig. 4.2. The RT-TDDFT simulations were carried out by Dr. Mitsuharu Uemoto and Prof. Kazuhiro Yabana who provided with Figs. 4.23 and 4.22. The optical pump-probe measurements were performed by the author supported by Prof. Simon Wall. The samples were provided by SM and TD supported by PS and the author.

# Publications

The work presented on this thesis concived the following publications:

**Chapter 2** Bárbara Buades, Iker León, Antonio Picón, Nicola Di Palo, Seth L. Cousin, Stephan M. Teichmann, Jens Biegert, *Tailoring soft X-ray attosecond pulses by phase matching manipulation*, in preparation.

**Chapter 3** Bárbara Buades, Dooshaye Moonshiram, Themistoklis P. H. Sidiropoulos, Iker León, Peter Schmidt, Irina Pi, Nicola Di Palo, Seth L. Cousin, Antonio Picón, Frank Koppens, Jens Biegert, Dispersive soft x-ray absorption fine-structure spectroscopy in graphite with an attosecond pulse, Optica 5, 502 - 506 (2018).

Bárbara Buades, Themistoklis P. H. Sidiropoulos, Azzedine Bendounan, Fausto Sirotti, Antonio Picón, John J. Rehr, Biplob Nandy, Samuel Mañas-Valero, Eugenio Coronado, Thomas Danz, Jens Biegert, *Attosecond Auger decay and its role in NEXAFS after core-shell excitation of $TiS_2$ and Graphite*, in preparation.

**Chapter 4** Bárbara Buades, Antonio Picón, Iker León, Nicola Di Palo, Seth L. Cousin, Caterina Cocchi, Eric Pellegrin, Javier Herrero-Martín, Samuel Mañas-Valero, Eugenio Coronado, Thomas Danz, Claudia Draxl, Mitsuharu Uemoto, Kazuhiro Yabana, Martin Schultze, Simon Wall, Jens Biegert, *Light-field-driven semimetal Bloch dynamics*, under review.

Other publications by the author during the PhD.:

- Seth L. Cousin, Nicola Di Palo, Bárbara Buades, Stephan M. Teichmann, Maurizio Reduzzi, Michele Devetta, Anatoli Kheifets, Giuseppe Sansone and Jens Biegert, Attosecond Streaking in the Water Window: A New Regime of Attosecond Pulse Characterization, Physical Review X 7, 041030 (2017)
- Seth L. Cousin, Francisco Silva, Stephan M. Teichmann, Michael Hemmer, Bárbara Buades and Jens Biegert, High-flux table-top soft x-ray source driven

by sub-2-cycle, CEP stable, 1.85-$\mu$m 1-kHz pulses for carbon K-edge spectroscopy, Optics Letters 39, 5383-5386 (2014)

# Bibliography


[1] Drescher, M. et al. Time-resolved atomic inner-shell spectroscopy. *Nature* **419**, 803–807 (2002).

[2] Uiberacker, M. et al. Attosecond real-time observation of electron tunnelling in atoms. *Nature* **446**, 627–632 (2007).

[3] Goulielmakis, E. et al. Real-time observation of valence electron motion. *Nature* **466**, 739–743 (2010).

[4] Schultze, M. et al. Delay in Photoemission. *Science* **328**, 5986 (2010).

[5] Wang, H. et al. Attosecond Time-Resolved Autoionization of Argon. *Physical Review Letters* **105**, 143002 (2010).

[6] Chini, M. et al. Subcycle ac Stark Shift of Helium Excited States Probed with Isolated Attosecond Pulses. *Physical Review Letters* **109**, 073601 (2012).

[7] Garg, M. et al. Multi-petahertz electronic metrology. *Nature* **538**, 359–363 (2016).

[8] Sabbar, M. et al. State-resolved attosecond reversible and irreversible dynamics in strong optical fields. *Nature Physics* **13**, 472–478 (2017).

[9] Hütten, K. et al. Ultrafast quantum control of ionization dynamics in krypton. *Nature Communications* **9**, 719 (2018).

[10] Sansone, G. et al. Electron localization following attosecond molecular photoionization. *Nature* **465**, 763–766 (2010).

[11] Wörner, H. J. et al. Charge migration and charge transfer in molecular systems. *Structural Dynamics* **4**, 061508 (2017).

[12] Young, L. et al. Roadmap of ultrafast x-ray atomic and molecular physics. *Journal of Physics B* **51**, 032003 (2018).

[13] Cattaneo, L. et al. Attosecond coupled electron and nuclear dynamics in dissociative ionization of H2. *Nature Physics* (2018).

[14] Cavalieri, A. L. et al. Attosecond spectroscopy in condensed matter. *Nature* **449**, 1029–1032 (2007).

[15] Schultze, M. et al. Controlling dielectrics with the electric field of light. *Nature* **493**, 75–78 (2013).

[16] Schultze, M. et al. Attosecond band-gap dynamics in silicon. *Science* **346**, 6215 (2014).

[17] Neppl, S. et al. Direct observation of electron propagation and dielectric screening on the atomic length scale. *Nature* **517**, 342–346 (2015).

[18] Lucchini, M. et al. Attosecond dynamical Franz-Keldysh effect in polycrystalline diamond. *Science* **353**, 6302 (2016).

[19] Sommer, A. et al. Attosecond real time observation of the nonlinear polarization and energy transfer in dielectrics. *Nature* **534**, 86–90 (2016).

[20] Moulet, A., Bertrand, J. B., Klostermann, T., Guggenmos, A. & Karpowicz, N. Soft x-ray excitonics. *Science* **357**, 6356 (2017).

[21] Schlaepfer, F. et al. Attosecond optical-field-enhanced carrier injection into the GaAs conduction band. *Nature Physics* (2018).

[22] Corkum, P. B., Burnett, N. H. & Ivanov, M. Y. Subfemtosecond pulses. *Optics letters* **19**, 1870–1872 (1994).

[23] Lewenstein, M., Balcou, P., Ivanov, M. Y., L'Huillier, A. & Corkum, P. B. Theory of high-harmonic generation by low-frequency laser fields. *Physical Review A* **49**, 2117 (1994).

[24] Paul, P. M. et al. Observation of a Train of Attosecond Pulses from High Harmonic Generation. *Science* **292**, 5522 (2001).

[25] Sansone, G. et al. Isolated Single-Cycle Attosecond Pulses. *Science* **314**, 443 (2006).

[26] Goulielmakis, E. et al. Single-Cycle Nonlinear Optics. *Science* **320**, 1614–1617 (2008).

[27] Zhao, K. et al. Tailoring a 67 attosecond pulse through advantageous. *Optics letters* **37**, 3891–3893 (2012).

[28] Shan, B. & Chang, Z. Dramatic extension of the high-order harmonic cutoff by using a long-wavelength driving field. *Physical Review A* **65**, 011804(R) (2001).

[29] Popmintchev, T., Chen, M.-c., Arpin, P., Murnane, M. M. & Kapteyn, H. C. The attosecond nonlinear optics of bright coherent X-ray generation. *Nature Photonics* **4**, 822–832 (2010).

[30] Li, J. et al. 53-attosecond X-ray pulses reach the carbon K-edge. *Nature Communications* **8**, 186 (2017).

[31] Guamnitz, T. et al. Streaking of 43-attosecond soft-X-ray pulses generated by a passively CEP-stable mid-infrared driver. *Optics Express* **25**, 27506–27518 (2017).

[32] Tate, J. et al. Scaling of wave-packet dynamics in an intense midinfrared Field. *Physical Review Letters* **98**, 013901 (2007).

[33] Frolov, M. V., Manakov, N. L. & Starace, A. F. Wavelength scaling of high-harmonic yield: Threshold phenomena and bound state symmetry dependence. *Physical Review Letters* **100**, 173001 (2008).

[34] Falcão-Filho, E. L., Gkortsas, M., Gordon, A. & Kärtner, F. X. Analytic scaling analysis of high harmonic generation conversion efficiency. *Optics Express* **17**, 11217–11219 (2009).

[35] Austin, D. R. & Biegert, J. Strong-field approximation for the wavelength scaling of high-harmonic generation. *Physical Review A* **86**, 023813 (2012).

[36] Ishii, N. et al. Carrier-envelope phase-dependent high harmonic generation in the water window using few-cycle infrared pulses. *Nature Communications* **5**, 3331 (2014).

[37] Suga, M. et al. Native structure of photosystem II at 1.95 Åresolution viewed by femtosecond X-ray pulses. *Nature* **517**, 99–103 (2014).

[38] Waldrop, M. M. X-ray science: The big guns. *Nature* **505**, 604–606 (2014).

[39] Silva, F., Teichmann, S. M., Cousin, S. L., Hemmer, M. & Biegert, J. Spatiotemporal isolation of attosecond soft X-ray pulses in the water window. *Nature Communications* **6**, 6611 (2015).

[40] Teichmann, S. M., Silva, F., Cousin, S. L., Hemmer, M. & Biegert, J. 0.5-keV Soft X-ray attosecond continua. *Nature Communications* **7**, 11493 (2016).

[41] Cousin, S. L. et al. Attosecond Streaking in the Water Window: A New Regime of Attosecond Pulse Characterization. *Physical Review X* **7**, 041030 (2017).

[42] Krause, J. L., Schafer, K. J. & Kulander, K. C. High-Order Harmonic Generation from Atoms and Ions in the High Intensity Regime. *Physical Review Letters* **68**, 3535 (1992).

[43] Stein, G. J. et al. Water-window soft x-ray high-harmonic generation up to the nitrogen K-edge driven by a kHz, 2.1 $\mu$ m OPCPA source. *Journal of Physics B* **49**, 155601 (2016).

[44] Johnson, A. S. et al. Measurement of sulfur L2,3 and carbon K edge XANES in a polythiophene film using a high harmonic supercontinuum. *Structural Dynamics* **3**, 062603 (2016).

[45] Popmintchev, T. et al. Bright Coherent Ultrahigh Harmonics in the keV X-ray Regime from Mid-Infrared Femtosecond Lasers. *Science* **336**, 1287 (2012).

[46] Marcus, G. et al. Subfemtosecond K-shell excitation with a few-cycle infrared laser field. *Physical Review Letters* **108**, 023201 (2012).

[47] Takahashi, E. J., Kanai, T. & Midorikawa, K. High-order harmonic generation by an ultrafast infrared pulse Efficient generation of a coherent "water window" X-ray. *Applied Physics B* **100**, 29–41 (2010).

[48] Chen, M.-C. et al. Bright, Coherent, Ultrafast Soft X-Ray Harmonics Spanning the Water Window from a Tabletop Light Source. *Physical Review Letters* **105**, 173901 (2010).

[49] Xiong, H. et al. Generation of a coherent x ray in the water window region at 1 kHz repetition rate using a mid-infrared pump source. *Optics letters* **34**, 1747–1749 (2009).

[50] Spielmann, C. et al. Generation of Coherent X-rays in the Water Window Using 5-Femtosecond Laser Pulses. *Science* **278**, 5338 (1997).

[51] Seres, E., Seres, J., Krausz, F. & Spielmann, C. Generation of coherent soft-X-ray radiation extending far beyond the titanium L edge. *Physical Review Letters* **92**, 163002 (2004).

[52] Seres, E., Seres, J. & Spielmann, C. Time resolved spectroscopy with femtosecond soft-x-ray pulses. *Applied Physics A* **96**, 43–50 (2009).

[53] Seres, J. et al. Laser-driven amplification of soft X-rays by parametric stimulated emission in neutral gases. *Nature Physics* **6**, 455–461 (2010).

[54] Seres, J. et al. High-harmonic generation and parametric amplification in the soft X-rays from extended electron trajectories. *Scientific reports* **4**, 4234 (2014).

[55] Cousin, S. L. et al. High-flux table-top soft x-ray source driven by sub-2-cycle, CEP stable, 185-$\mu$m 1-kHz pulses for carbon K-edge spectroscopy. *Optics Letters* **39**, 5383–5386 (2014).

[56] Hentschel, M. et al. Attosecond metrology. *Nature* **414**, 509–513 (2001).

[57] Hassan, M. T. et al. Optical attosecond pulses and tracking the nonlinear response of bound electrons. *Nature* **530**, 66–70 (2016).

[58] Sola, I. J. et al. Controlling attosecond electron dynamics by phase-stabilized polarization gating. *Nature Physics* **2**, 319–322 (2006).

[59] Antoine, P., Huillier, A. L., Lewenstein, M. & Salie, P. Theory of high-order harmonic generation by an elliptically polarized laser field. *Physical Review A* **53**, 1725 (1996).

[60] Xu, H. et al. Wavelength scaling of elliptical-polarization dependence of high-order harmonic generation. *Optics letters* **35**, 472–474 (2010).

[61] Mashiko, H. et al. Double Optical Gating of High-Order Harmonic Generation with Carrier-Envelope Phase Stabilized Lasers. *Physical Review Letters* **100**, 103906 (2008).

[62] Kienberger, R. et al. Atomic transient recorder. *Nature* **427**, 817–821 (2004).

[63] Frank, F. et al. Invited review article: technology for attosecond science. *The Review of scientific instruments* **83**, 071101 (2012).

[64] Vincenti, H. & Quéré, F. Attosecond Lighthouses: How To Use Spatiotemporally Coupled Light Fields To Generate Isolated Attosecond Pulses. *Physical Review Letters* **108**, 113904 (2012).

[65] Kim, K. T. et al. Photonic streaking of attosecond pulse trains. *Nature Photonics* **7**, 651–656 (2013).

[66] Jullien, A. et al. Ionization phase-match gating for wavelength-tunable isolated attosecond pulse generation. *Applied Physics B* **93**, 433 (2008).

[67] Hammond, T. J., Brown, G. G., Kim, K. T., Villeneuve, D. M. & Corkum, P. B. Attosecond pulses measured from the attosecond lighthouse. *Nature Photonics* **10**, 171–175 (2016).

[68] Chen, M.-C. et al. Generation of bright isolated attosecond soft X-ray pulses driven by multicycle midinfrared lasers. *Proceedings of the National Academy of Sciences of the United States of America* **111**, (23) E2361–E2367 (2014).

[69] Ferrari, F. et al. High-energy isolated attosecond pulses generated by above-saturation few-cycle fields. *Nature Photonics* **4**, 875–879 (2010).

[70] Schmidt, B. E. et al. Compression of 1.8$\mu$m laser pulses to sub two optical cycles with bulk material. *Applied Physics Letters* **96**, 121109 (2010).

[71] Haworth, C. A. et al. Half-cycle cutoffs in harmonic spectra and robust carrier-envelope phase retrieval. *Nature Physics* **3**, 52–57 (2007).

[72] Baltuška, A. et al. Attosecond control of electronic processes by intense light fieds. *Nature* **421**, 611–615 (2003).

[73] Nisoli, M. et al. Effects of Carrier-Envelope Phase Differences of Few-Optical-Cycle Light Pulses in Single-Shot High-Order-Harmonic Spectra. *Physical Review Letters* **91**, 213905 (2003).

[74] Cousin, S. L. *Towards the Generation of Isolated Attosecond Pulses in the Water Window*. Ph.D. thesis, Universitat Politècnica de Catlaunya (2016).

[75] Austin, D. R. & Biegert, J. Attosecond pulse shaping using partial phase matching. *New Journal of Physics* **16**, 113011 (2014).

[76] Gaarde, M. B. et al. Spatiotemporal separation of high harmonic radiation into two quantum path components. *Physical Review A* **59**, 1367 (1999).

[77] Teichmann, S. M. *Ponderomotively scaled high harmonic generation for attoscience in the water window by*. Ph.D. thesis, Universitat Politècnica de Catlaunya (2015).

[78] Dubrouil, A. et al. Spatio-spectral structures in high-order harmonic beams generated with Terawatt 10-fs pulses. *Nature Communications* **5**, 4637 (2014).

[79] Sun, H.-W. et al. Extended phase matching of high harmonic generation by plasma-induced defocusing. *Optica* **4**, 976–981 (2017).

[80] Gauthier, D. et al. Tunable orbital angular momentum in high-harmonic generation. *Nature Communications* **8**, 14971 (2017).

[81] Witting, T. et al. Characterization of high-intensity sub-4-fs laser pulses using spatially encoded spectral shearing interferometry. *Optics Letters* **36**, 1680–1682 (2011).

[82] Hernández-García, C. et al. Isolated broadband attosecond pulse generation

with near- and mid-infrared driver pulses via time-gated phase matching. *Optics Express* **25**, 875–879 (2017).

[83] Rudawski, P. et al. A high-flux high-order harmonic source. *Review of Scientific Instruments* **84**, 073103 (2013).

[84] Niu, Y. et al. Pressure-dependent phase matching for high harmonic generation of Ar and N2 in the tight focusing regime. *Optics Communications* **397**, 118–121 (2017).

[85] Lewenstein, M., Salieres, P. & L'Huillier, A. Phase of the atomic polarization in high-order harmonic generation. *Physical Review A* **52**, 4747 (1995).

[86] Tong, X. M. & Lin, C. D. Empirical formula for static field ionization rates of atoms and molecules by lasers in the barrier-suppression regime. *Journal of Physics B: Atomic, Molecular and Optical Physics* **38**, 2593–2600 (2005).

[87] Le, A. T., Lucchese, R. R. & Lin, C. D. Quantitative rescattering theory of high-order harmonic generation for polyatomic molecules. *Physical Review A* **80**, 013401 (2009).

[88] Geissler, M. et al. Light Propagation in Field-Ionizing Media: Extreme Nonlinear Optics. *Physical Review Letters* **83**, 2930 (1999).

[89] Couairon, A. & Mysyrowicz, A. Femtosecond filamentation in transparent media. *Physics Reports* **441**, 47–189 (2007).

[90] Zaïr, A. et al. Spatio-temporal characterization of few-cycle pulses obtained by filamentation. *Optics Express* **15**, 5394 (2007).

[91] Sayers, D. E., Stern, E. A. & Lytle, F. New Technique for Investigating Noncrystalline Structures: Fourier Analysis of the Extended X-Ray— Absorption Fine Structure. *Physical Review Letters* **27**, 1204 (1971).

[92] Hähner, G. Near edge X-ray absorption fine structure spectroscopy as a tool to probe electronic and structural properties of thin organic films and liquids. *Chemical Society Reviews* **35**, (12):1244–55 (2006).

[93] Sauer, K., Yano, J. & Yachandra, V. K. X-ray spectroscopy of the photosynthetic oxygen-evolving complex. *Coordination Chemistry Reviews* **252**, 318–335 (2008).

[94] Ade, H. & Stoll, H. Near-edge X-ray absorption fine-structure microscopy of organic and magnetic materials. *Nature Materials* **8**, 281–290 (2009).

[95] Frahm, R. Quick scanning exafs: First experiments. *Nuclear Inst. and Methods in Physics Research, A* **270**, 578–581 (1988).

[96] Dobson, B. R. Quick Scanning EXAFS Facilities at Daresbury SRS. *Synchrotron Radiation News* **7**, 21–24 (1994).

[97] Vacher, M., Steinberg, L., Jenkins, A. J., Bearpark, M. J. & Robb, M. A. Electron dynamics following photoionization: Decoherence due to the nuclear-wave-packet width. *Physical Review A* **92**, 040502(R) (2015).

[98] Schoenlein, R. W. et al. Generation of femtosecond pulses of synchrotron radiation. *Science* **287**, 5461 (2000).

[99] L'Huillier, A., Lompre, L. A., Mainfray, G. & Manus, C. Multiply charged ions formed by multiphoton absorption processes in the continuum. *Physical Review Letters* **48**, 1814 (1982).

[100] McPherson, A. et al. Studies of multiphoton production of vacuum-ultraviolet radiation in the rare gases. *Journal of the Optical Society of America B* **4**, 595 (1987).

[101] Thompson, A. C. et al. *X-RAY DATA BOOKLET* (Berkeley, California, 2001).

[102] Newville, M. Fundamentals of XAFS. *Reviews in Mineralogy and Geochemistry* **78** (2014).

[103] Ade, H. et al. X-RAY DATA BOOKLET. *Physical Review Letters* **8**, 186 (2014).

[104] Koningsberger, D. C. *Prins, R. X Ray Absorption: Principles, Applications, Techniques of EXAFS, SEXAFS and XANES* (John Wiley & Sons, 1988).

[105] Krause, M. O. & Oliver, J. H. Natural width of atomic K and L level K[alpha] X-ray lines and several KLL Auger lines. (1979).

[106] Young, L. et al. Femtosecond electronic response of atoms to ultra-intense X-rays. *Nature* **466**, 56–61 (2010).

[107] Apostolova, T. & Oliva, E. Combined Quantum Kinetic and Rate Equations Modeling of the Non-Equilibrium Carrier Dynamics of Matter Exposed to X-Ray Laser Pulses. *Bulgarian Journal of Physics* **44**, 509–519 (2017).

[108] Shkvarin, A. S. et al. Electronic structure of titanium dichalcogenides TiX2 (X = S, Se, Te). *Journal of Experimental and Theoretical Physics* **114**, 150–156 (2012).

[109] Sanchez-Gonzalez, A. et al. Auger electron and photoabsorption spectra of glycine in the vicinity of the oxygen K-edge measured with an X-FEL. *Journal of Physics B: Atomic, Molecular and Optical Physics* **48**, 234004 (2015).

[110] Eads, C. N., Bandak, D., Neupane, M. R., Nordlund, D. & Monti, O. L. Anisotropic attosecond charge carrier dynamics and layer decoupling in quasi-2D layered. *Nature Communications* **8**, 1369 (2017).

[111] Wickramasinghe, N. C., Lukes, T. & Dempsey, M. J. Mean free path limitation of conduction electrons and extinction efficiencies of graphite grains. *Astrophysics and Space Science* **30**, 315–325 (1974).

[112] Barrett, N., Krasovskii, E. E., Themlin, J. M. & Strocov, V. N. Elastic scattering effects in the electron mean free path in a graphite overlayer studied by photoelectron spectroscopy and LEED. *Physical Review B* **71**, 035427 (2005).

[113] Gall, D. Electron mean free path in elemental metals. *Journal of Applied Physics* **119**, 095101 (2016).

[114] Heske, C. et al. Band widening in graphite. *Physical Review B* **59**, 4680 (1999).

[115] Girifalco, L. A. & Hodak, M. Van der Waals binding energies in graphitic structures. *Physical Review B* **65**, 125404 (2002).

[116] Reich, S. & Thomsen, C. Raman spectroscopy of graphite. *Philosophical Transactions of the Royal Society A* **362**, 2271–2288 (2004).

[117] Marinopoulos, A. G., Reining, L., Rubio, A. & Olevano, V. Ab initio study of the optical absorption and wave-vector-dependent dielectric response of graphite. *Physical Review B* **69**, 245419 (2004).

[118] Bučko, T., Lebègue, S., Hafner, J. & Ángyán, J. G. Tkatchenko-Scheffler van der Waals correction method with and without self-consistent screening applied to solids. *Physical Review B* **87**, 064110 (2013).

[119] Ooi, N., Rairkar, A. & Adams, J. B. Density functional study of graphite bulk and surface properties. *Carbon* **44**, 231–242 (2006).

[120] Castellanos-Gomez, A. et al. Deterministic transfer of two-dimensional materials by all-dry viscoelastic stamping. *2D Materials* **1**, 011002 (2014).

[121] Guerra, C. F., Snijders, J., te Velde, G. & Baerends, E. J. Towards an order-N DFT method. *Theor. Chem. Acc.* **99:391** (1998).

[122] te Velde, G. et al. Chemistry with ADF. *Journal of Computational Chemistry* **22**, 931–967 (2001).

[123] Vrije Universiteit, Amsterdam, T. N. ADF2017, SCM, Theoretical Chemistry (2016).

[124] Van Lenthe, E. & Baerends, E. J. Optimized Slater-Type Basis Sets for the Elements 1 – 118. *J. Comput. Chem.* **24**, 1142–1156 (2003).

[125] Rosenberg, R. A., Love, P. J. & Rehn, V. Polarization-dependent C(K) near-edge x-ray-absorption fine structure of graphite. *Physical Review B* **33**, 4034 (1986).

[126] Brühwiler, P. A. et al. pi* and sigma* excitons in C- 1s absorption of graphite. *Physical Review Letters* **74**, 614 (1995).

[127] Ahuja, R. et al. Theoretical and experimental study of the graphite 1s x-ray absorption edges. *Physical Review B* **54**, 14396 (1996).

[128] Hemraj-Benny, T. et al. Near-edge X-ray absorption fine structure spectroscopy as a tool for investigating nanomaterials. *Small* **2**, 26–35 (2006).

[129] Watts, B., Thomsen, L. & Dastoor, P. C. Methods in carbon K-edge NEXAFS: Experiment and analysis. *Journal of Electron Spectroscopy and Related Phenomena* **151**, 105–120 (2006).

[130] Brandes, J. A. et al. Carbon K-edge XANES spectromicroscopy of natural graphite. *Carbon* **46**, 1424–1434 (2008).

[131] Papagno, M. et al. Polarization-dependent C K near-edge X-ray absorption fine-structure of graphene. *Chemical Physics Letters* **475**, 269–271 (2009).

[132] Schultz, B. J. et al. Imaging local electronic corrugations and doped regions in graphene. *Nature communications* **2**, 372 (2011).

[133] Ravel, B. & Newville, M. ATHENA, ARTEMIS, HEPHAESTUS: data analysis for X-ray absorption spectroscopy using IFEFFIT. *J. Synchrotron Rad.* **12**, 537–541 (2005).

[134] Rehr, J. J., Kas, J. J., Vila, F. D., Prange, M. P. & Jorissen, K. Parameter-free calculations of X-ray spectra with FEFF9. *Physical Chemistry Chemical Physics* **12**, 5503–5513 (2010).

[135] Rehr, J. J. & Albers, R. C. Theoretical approaches to x-ray absorption fine structure. *Reviews of Modern Physics* **72**, 621 (2000).

[136] Tanaka, T., Matsubayashi, N., Imamura, M. & Shimada, H. Synchronous scanning of undulator gap and monochromator for XAFS measurements in soft x-ray region. *Journal of Synchrotron Radiation* **8**, 345–347 (2001).

[137] Comelli, G., Stöhr, J. & Jark, W. Extended x-ray-absorption fine-structure studies of diamond and graphite. *Physical Review B* **37**, 4383–4389 (1988).

[138] Bassett, P. J. & Gallon, T. E. The effect of oxidation on the high resolution Auger spectrum of titanium. *Journal of Electron Spectroscopy and Related Phenomena* **2**, 101–104 (1973).

[139] Allen, G. C., Tucker, P. M. & Wild, R. K. High resolution LMM auger electron spectra of some first row transition elements. *Surface Science* **68**, 469–478 (1977).

[140] Fuggle, J. C. & Alvandro, S. F. Core-level lifetimes as determined by x-ray photoelectron spectroscopy measurements. *Physical Review A* **22**, 1615 (1980).

[141] de Groot, F. M. F., Fuggle, J. C., Thole, B. T. & Sawatzky, G. A. L2,3 x-ray-absorption edges of d0 compounds: K+, Ca2+, Sc3+, and Ti4+ in Oh (octahedral) symmetry. *Physical Review B* **41**, 928 (1990).

[142] Nyholm, R., Martensson, N., Lebugle, A. & Axelsson, U. Auger and Coster-Kronig broadening effects in the 2p and 3p photoelectron spectra from the metals 22Ti-30Zn. *Journal of Physics F: Metal Physics* **11**, 1727–33 (1981).

[143] Simunek, A., Sipr, O., Bocharov, S., Heumann D. & Gräger, G. Unoccupied electron states of TiS2 studied by means of polarized x-ray absorption. *Physical Review B* **56**, 232 (1997).

[144] Buades, B. et al. Dispersive soft x-ray absorption fine-structure spectroscopy in graphite with an attosecond pulse. *Optica* **5**, 502 – 506 (2018).

[145] Powell, J. R. The Quantum Limit to Moore's Law. *Proceedings of the IEEE* **96**, 1247–1248 (2008).

[146] Markov, I. L. Limits on fundamental limits to computation. *Nature* **512**, 147–154 (2014).

[147] Hemminger, J. C. Challenges at the Frontiers of Matter and Energy: Transformative Opportunities for Discovery Science. *Basic Energy Sciences Advisory Committee* (2015).

[148] Pertot, Y. et al. Time-resolved x-ray absorption spectroscopy with a water window high-harmonic source. *Science* **6114**, 1126 (2017).

[149] Schiffrin, A. et al. Optical-field-induced current in dielectrics. *Nature* **493**, 70–74 (2013).

[150] Mashiko, H., Oguri, K., Yamaguchi, T., Suda, A. & Gotoh, H. Petahertz optical drive with wide-bandgap semiconductor. *Nature Physics* **12**, 741–746 (2016).

[151] Zürch, M. et al. Direct and simultaneous observation of ultrafast electron and hole dynamics in germanium. *Nature Communications* **8**, 15734 (2017).

[152] Zürch, M. et al. Ultrafast carrier thermalization and trapping in silicon-germanium alloy probed by extreme ultraviolet transient absorption spectroscopy. *Structural Dynamics* **4**, 044029 (2017).

[153] Kittel, C. *Introduction to Solid State Physics* (2004), 8th edn.

[154] Geim, A. K. & Grigorieva, I. V. Van der Waals heterostructures. *Nature* **499**, 419–425 (2013).

[155] Jariwala, D., Marks, T. J. & Hersam, M. C. Mixed-dimensional van der Waals heterostructures. *Nature Materials* **16**, 170–181 (2016).

[156] Lin, Z. et al. 2D materials advances: from large scale synthesis and controlled heterostructures to improved characterization techniques, defects and applications. *2D Materials* **3**, 042001 (2016).

[157] Novoselov, K. S., Mishchenko, A., Carvalho, A., Neto, A. H. C. & Road, O. 2D materials and van der Waals heterostructures. *Science* **353**, 6298 (2016).

[158] Watanabe, K., Taniguchi, T. & Kanda, H. Direct-bandgap properties and evidence for ultraviolet lasing of hexagonal boron nitride single crystal. *Nature materials* **3**, 404–409 (2004).

[159] Li, Z. & Gao, F. Structure, bonding, vibration and ideal strength of primitive-centered tetragonal boron nitride. *Phys. Chem. Chem. Phys.* **14**, 869–876 (2012).

[160] Banerjee, S. & Pat, S. K. Criticality of Surface Topology for Charge-carrier Transport Characteristics in Two-Dimensional Borocarbonitrides: Design Principle of an Efficient Electronic Material. *Nanoscale* **6**, 13430–13434 (2014).

[161] Fang, C. M., de Groot, R. A. & Haas, C. Bulk and surface electronic structure of 1T-TiS2 and 1T-TiSe2. *Physical Review B* **56**, 265 (1997).

[162] Xu, M., Liang, T., Shi, M. & Chen, H. Graphene-Like Two-Dimensional Materials. *Chemical Review* **113**, 3766–3798 (2013).

[163] Chen, P. et al. Charge density wave transition in single-layer titanium diselenide. *Nature Communications* **6**, 8943 (2015).

[164] Scanlon, D. O. et al. Band alignment of rutile and anatase TiO2. *Nature materials* **12**, 798–801 (2013).

[165] Shin, S. et al. Vacuum-ultraviolet reflectance and photoemission study of the metal-insulator phase transitions in VO2, V6O13, and V2O3. *Physical Review B* **41**, 4993 (1990).

[166] Laubach, S. et al. Theoretical and experimental determination of the electronic structure of V(2)O(5), reduced V(2)O(5-x) and sodium intercalated NaV(2)O(5). *Physical Chemistry Chemical Physics* **9**, 2564–76 (2007).

[167] Patel, K. R., Vaidya, R. D., Dave, M. S. & Patel, S. G. Crystal structure and band gap measurements of vanadium diselenide single crystals. *Sciencia Acta Xaveriana* **1**, 5–15 (2009).

[168] Hossain, J., Julkarnain, M., Sharif, K. S. & Khan, K. A. Optical Properties of E-beam Evaporated Indium Selenide ( InSe ) Thin Films. *JSRR* **3(12)**, 1642–1655 (2014).

[169] Marsillac, S., Mangale, N., Gade, V. & Khare, S. Structural and electronic properties of $\beta$-In2X3 (X=O, S, Se, Te) using ab initio calculations. *Thin Solid Films* **519**, 5679–5683 (2011).

[170] Bletskan, D. I., Frolova, V. V. & Glukhov, K. E. Electronic Structure of 18 R-SnS2 crystal. *Journal of Optoelectronics and advanced materias* **12**, (11):2236–2241 (2010).

[171] Kumar, a. & Ahluwalia, P. K. Electronic structure of transition metal dichalcogenides monolayers 1H-MX2 (M = Mo, W; X = S, Se, Te) from ab-initio theory: new direct band gap semiconductors. *The European Physical Journal B* **85**, 186 (2012).

[172] Rao, M., Ravindranadh, K., Kasturi, A. & Shekhawat, M. Structural Stoichiometry and Phase Transitions of MoO3 Thin Films for Solid State Microbatteries. *Res. J. Recent Sci.* **2(4)**, 67–73 (2013).

[173] Kadantsev, E. S. & Hawrylak, P. Electronic structure of a single MoS2 monolayer. *Solid State Communications* **152**, 909–913 (2012).

[174] Ze-jin, Y. et al. Electronic structure and optical properties of rutile RuO2 from first principles. *Chin. Phys. B* **19**, 7, 077102 (2010).

[175] Ibarz, A., Ruiz, E. & Alvarez, S. Electronic Structure of Host Lattices for Intercalation Compounds: SnS2, SNSe2, ZrSe2 and TaS2. *Chem. Mater.* **10**, 3422–3428 (1998).

[176] Singh, T., Kumar, J. & Sastri, O. S. K. S. Effect of strain along C-axis NbS2. *AIP Conference Proceedings* **1661**, 110024 (2015).

[177] Chen, L. et al. First-principles calculations on structural, electronic properties of V-doped 2H-NbSe2. *RSC Advances* **4**, 9573 (2014).

[178] Traving, M. et al. Combined photoemission and inverse photoemission study of HfS2. *Physical Review B* **63**, 035107 (2001).

[179] Sharma, S. et al. Electronic structure of 1T-TiS2. *Physical Review B* **59**, 833 (1999).

[180] Reshak, A. H., Kityk, I. V. & Auluck, S. Electronic structure and optical properties of 1T-TiS2 and lithium intercalated 1T-TiS2 for lithium batteries. *The Journal of Chemical Physics* **129**, 074706 (2008).

[181] Whittingham, M. S. Lithium Batteries and Cathode Materials. *Chemical Review* **104**, 4271–4301 (2004).

[182] Reshak, A. H. Copper-Intercalated TiS2: Electrode Materials for Rechargeable Batteries as Future Power Resources. *J. Phys. Chem. A.* **113**, 1635–1645 (2009).

[183] Chen, J., Li, S.-l., Tao, Z.-l., Shen, Y.-t. & Cui, C.-x. Titanium Disulfide Nanotubes as Hydrogen-Storage Materials. *J. Am. Chem. Soc.* **125**, 5284–5285 (2003).

[184] Liu, X. et al. High Performance Field-Effect Transistor Based on Multilayer Tungsten Disulfide. *ACS nano* **8**, (10) 10396–10402 (2014).

[185] Cucinotta, C. S. et al. Electronic Properties and Chemical Reactivity of TiS <sub>2</sub> Nanoflakes. *The Journal of Physical Chemistry C* **119**, 15707–15715 (2015).

[186] Inoue, M., Hughes, H. P. & Yoffe, A. D. The electronic and magnetic properties of the 3d transition metal intercalates of TiS2 (1989).

[187] Dolui, K. & Sanvito, S. Dimensionality-driven phonon softening and incipient charge density wave instability in TiS 2. *EPL* **115**, 47001 (2016).

[188] Greenaway, D. L. & Nitsche, R. Preparation and optical properties of group IV–VI2 chalcogenides having the CdI2 structure (1965).

[189] Klipstein, P. C., Bagnall, A. G., Liang, W. Y., Marseglia, E. A. & Friend, R. H. Stoichiometry dependence of the transport properties of TiS 2. *Journal of Physics C: Solid State Physics* **14**, 4067 (1981).

[190] Liu, B. et al. Electronic structure of TiS2 and its electric transport properties under high pressure. *Journal of Applied Physics* **109**, 053717 (2011).

[191] Xu, C., Brown, P. A. & Shuford, K. L. Strain-induced semimetal-to-semiconductor transition and indirect-to-direct band gap transition in monolayer 1T-TiS 2. *RSC Advances* **5**, 83876 (2015).

[192] Hohenberg, P. & Kohn, W. Inhomogeneous Electron gas. *Physical Review* **136**, B864 (1964).

[193] Kohn, W. & Sham, L. J. Self-Consistent Equations Including Exchange and Correlation Effects. *Physical Review* **140**, A1133 (1965).

[194] Gulans, A. et al. exciting: a full-potential all-electron package implementing density-functional theory and many-body perturbation theory. *Journal of Physics: Condensed Matter* **26**, 363202 (2014).

[195] Chianelli, R. R., Scanlon, J. C. & Thompson, A. H. Structure refinement of stoichiometric TiS 2. *Materials Research Bulletin* **10**, 1379–1382 (1975).

[196] Smith, G. S. & Snyder, R. L. FN: A criterion for rating powder diffraction patterns and evaluating the reliability of powder-pattern indexing. *Journal of Applied Crystallography* **12**, 60–65 (1979).

[197] Stohr, J., Sette, F. & Johnson, A. L. Near-Edge Xray Absorption Fine Structure Studies of Chemisorbed Hydrocarbons: Bond Lengths with a Ruler. *Physical Review Letters* **53**, 1684 (1984).

[198] Bressler, C. & Chergui, M. Ultrafast X-ray Absorption Spectroscopy. *Chemical Review* **104**, 1781–1812 (2004).

[199] Chergui, M. & Zewail, A. H. Electron and X-ray methods of ultrafast structural dynamics: Advances and applications. *ChemPhysChem* **10**, 28–43 (2009).

[200] El-Kouch, H., EL Farh, L., Sayah, J. & Challioui, A. Electronic and Optical Properties of TiS2 Determined from Generalized Gradient Approximation Study Electronic and Optical Properties of TiS 2 Determined from Generalized Gradient Approximation Study. *Chin. Phys. Lett.* **32**, 9, 096102 (2015).

[201] Yabana, K., Sugiyama, T., Shinohara, Y., Otobe, T. & Bertsch, G. F. Time-dependent density functional theory for strong electromagnetic fields in crystalline solids. *Physical Review B* **85**, 045134 (2012).

[202] Feldkamp, L., Shinozaki, S., Kukkonen, C. & Faile, S. Electron energy-loss spectroscopy of TiS2. *Physical Review B* **19**, 2291 (1979).

[203] Vorwerk, C., Cocchi, C. & Draxl, C. LayerOptics: Microscopic modeling of optical coefficients in layered materials. *Computer Physics Communications* **201**, 119–125 (2016).

[204] von Pauli, W. Über den Zusammenhang des Abschlusses der Elektronengruppen im Atom mit der Komplexstruktur der Spektren. *Zeitschrift für Phys.* **31**, 765–783 (1925).

[205] Liu, H. et al. High-harmonic generation from an atomically thin semiconductor. *Nature Physics* **13**, 262–265 (2016).

[206] Perdew, J. P., Burke, K. & Ernzerhof, M. Generalized Gradient Approximation Made Simple. *Physical Review Letters* **77**, 3865 (1996).

[207] Floss, I. et al. http://salmon-tddft.jp (2017).

[208] Ambrosch-Draxl, C. & Sofo, J. O. Linear optical properties of solids within the full-potential linearized augmented planewave method. *Computer Physics Communications* **175**, 1–14 (2006).

[209] McDonald, C. R., Vampa, G., Corkum, P. B. & Brabec, T. Intense-Laser Solid State Physics: Unraveling the Difference between Semiconductors and Dielectrics. *Physical Review Letters* **118**, 173601 (2017).

[210] Wu, M., Chen, S., Camp, S., Schafer, K. J. & Gaarde, M. B. Theory of strong-field attosecond transient absorption. *Journal of Physics B* **49**, 062003 (2016).

[211] Ott, C. et al. Lorentz meets Fano in spectral line shapes: a universal phase and its laser control. *Science* **340**, 716 (2013).

[212] Fano, U. Effect of configuration Interaction on intensities and phase shifts. *Physical Review* **124**, 1866 (1961).

[213] Föhlisch, A. et al. Direct observation of electron dynamics in the attosecond domain. *Nature* **436**, 373–376 (2005).

[214] Keldysh, L. V. Ionization on the field of a strong electromagnetic wave. *Soviet Physics JETP* **20**, 1307–1314 (1965).

[215] Jauho, A. P. & Johnsen, K. Dynamical franz-keldysh effect. *Physical Review Letters* **76**, 4576 (1996).

[216] Picón, A. Time-dependent Schrödinger equation for molecular core-hole dynamics. *Physical Review A* **95**, 023401 (2017).

[217] Haug, H. & Jauho, A.-P. *Quantum kinetics in transport and optics of semiconductors, Volume 6* (London, 1965), 2005 edn.

[218] Gaarde, M. B., Buth, C., Tate, J. L. & Schafer, K. J. Transient absorption and reshaping of ultrafast XUV light by laser-dressed helium. *Physical Review A* **83**, 013419 (2011).

[219] Wall, S. et al. Tracking the evolution of electronic and structural properties of VO 2 during the ultrafast photoinduced insulator-metal transition. *Physical Review B* **87**, 115126 (2013).

[220] Cavalleri, A. et al. Band-Selective Measurements of Electron Dynamics in VO2 Using Femtosecond Near-Edge X-Ray Absorption. *Physical Review Letters* **95**, 067405 (2005).

[221] Rini, M. et al. Transient electronic structure of the photoinduced phase of Pr0.7Ca0.3MnO3 probed with soft x-ray pulses. *Physical Review B* **80**, 155113 (2009).

[222] Breusing, M., Ropers, C. & Elsaesser, T. Ultrafast Carrier Dynamics in Graphite. *Physical Review Letters* **102**, 086809 (2009).